Numerical Assessment of Turbulence-Cascade Noise Reduction and Aerodynamic Penalties from Serrations

Martin Buszyk, Cyril Polacsek, Thomas Le Garrec, Raphaël Barrier, Christophe Bailly

Numerical Assessment of Turbulence-Cascade Noise Reduction and Aerodynamic Penalties from Serrations

Martin Buszyk,* Cyril Polacsek,† and Thomas Le Garrec‡
DAAA, ONERA, Université Paris-Saclay, 92320 Châtillon, France
Raphaël Barrier§
DAAA, ONERA, Université Paris-Saclay, 92190 Meudon, France
and
Christophe Bailly¶
Ecole Centrale de Lyon, 69130 Ecully, France

This work is related to the investigation of innovative stator designs aiming to reduce the dominant interaction noise in aeroengines. The study of turbulent structures definition is crucial for the accurate prediction of broadband noise radiation from passive treatments, as leading-edge serrations studied here. A modified Fourier modes-based methodology is proposed to obtain a fully three-dimensional incompressible turbulence field, while taking into account periodic and wall-boundary conditions. A low-noise geometry is examined along with the reference profile on a rectilinear seven-vane cascade rig using a hybrid computational fluid dynamics/computational aeroacoustics method. Numerically assessed noise reductions from the serrated airfoils are favorably compared with an analytical solution and a semi-empirical law. An overall sound power-level reduction around 4 to 6 dB is obtained at three acoustic certification points. Finally, the aerodynamic performances are also evaluated through Reynolds-averaged Navier–Stokes computations, and an improved variant of the initial treatment is proposed, allowing for acceptable penalties at the aerodynamic design point.

Nomenclature

c	=	chord of the airfoil
E	=	energy spectrum of turbulence
$f_{\min}$, $f_{\max}$	=	respectively, minimal and maximal considered frequencies
f_w	=	window function
g_w	=	correction function
h_s	=	amplitude of the serrations
$\boldsymbol{k}$	=	wave vector
k	=	norm of the wave vector $\boldsymbol{k}$
$(\boldsymbol{k_a}, \boldsymbol{k_b}, \boldsymbol{k_c})$	=	a specific orthonormal basis in the wave vector space
(k_x, k_y, k_z)	=	coordinates of the wave vector $\boldsymbol{k}$ in the basis $(\boldsymbol{x}, \boldsymbol{y}, \boldsymbol{z})$
(k_ξ, k_η, k_z)	=	coordinates of the wave vector $\boldsymbol{k}$ in the basis $(\boldsymbol{\xi}, \boldsymbol{\eta}, \boldsymbol{z})$
$\boldsymbol{k}^\perp$	=	wave vector component in the plane perpendicular to the z axis
L_w	=	input parameter defining the shape of the window function f_w
L_y	=	length in the computational aeroacoustics setup between the two sides of the periodic boundary condition
L_z	=	span of the airfoil
$L_{\xi\xi}$	=	integral longitudinal length scale of turbulence
n_v	=	number of vanes in the computational aeroacoustics domain
p, p_0, p'	=	fluid static, mean, fluctuating pressure
R_w	=	ratio between the length L_w (parameter of the window function f_w) and the span L_z
s	=	intervane spacing
St	=	Strouhal number of the serrations, where St equals frequency $\times\, h_s/U$
t	=	time
t_1	=	an arbitrary time interval
$\boldsymbol{U}$	=	mean velocity vector
$\boldsymbol{u}$, $\boldsymbol{u}'$	=	velocity vector, fluctuating velocity vector
$\boldsymbol{X}$	=	position vector in the physical space
$(\boldsymbol{x}, \boldsymbol{y}, \boldsymbol{z})$	=	orthonormal basis in the computational aeroacoustics setup frame, where $\boldsymbol{y}$ is aligned with the cascade and $\boldsymbol{z}$ with the span
α	=	a random angle in $[0, 2\pi]$
β_c	=	entrance flow angle with respect to x axis
Δf	=	frequency spacing
Δk	=	wave number discretization step (for each respective direction)
λ_s	=	serration wavelength
$(\boldsymbol{\xi}, \boldsymbol{\eta}, \boldsymbol{z})$	=	orthonormal basis in the inflow frame, where $\boldsymbol{\xi}$ aligned with the upstream flow and $\boldsymbol{z}$ with the span
ρ, ρ_0, ρ'	=	fluid, mean, fluctuating density
$\boldsymbol{\sigma}$	=	unit vector defining the direction of a given velocity fluctuation
φ_{ii}^{3D}, φ_{ii}^{2D}, φ_{ii}^{1D}	=	three-dimensional, two-dimensional (planar), one-dimensional autocorrelation velocity spectra along $_i$ direction
ψ	=	random phase in $[0, 2\pi]$
ω	=	angular frequency
ω'	=	vorticity of fluctuating velocity
$_i$	=	indices/subscripts denoting a direction, such as i equals ξ, denoting mean flow direction

*Ph.D. Candidate, Aerodynamics Aeroelasticity Aeroacoustics Department; martin.buszyk@onera.fr.
†Senior Research Engineer, Aerodynamics Aeroelasticity Aeroacoustics Department; cyril.polacsek@onera.fr.
‡Research Engineer, Aerodynamics Aeroelasticity Aeroacoustics Department; thomas.le_garrec@onera.fr.
§Research Engineer, Aerodynamics Aeroelasticity Aeroacoustics Department; raphael.Barrier@onera.fr.
¶Professor, University of Lyon, Institut National des Sciences Appliquées de Lyon, University Claude Bernard Lyon I, Laboratoire de Mécanique des Fluides et d'Acoustique, LMFA UMR 5509; christophe.bailly@ec-lyon.fr. Senior Member AIAA.

$\langle\rangle$	=	set average operation
z_{min}, z_{max}	=	respectively, coordinates of the bottom and top walls in the numerical setup

I. Introduction

IN ORDER to lower the turbofan engine noise emission, much effort is put into reducing the rotor/stator interaction noise sources, which are the dominant contributions for both tonal and broadband noise components particularly at approach (APP) condition. With this perspective, research projects have been set up, such as InnoSTAT in the framework of the H2020 European programs. The goal is to study promising passive and active technologies that might be implemented in future innovative stators. ONERA is involved in the design of a successful passive concept based on leading-edge serrations [1,2]. A set of these serrated low-noise vanes will be evaluated during the first test campaign of the InnoSTAT project, which will take place at Ecole Centrale de Lyon (ECL). Two numerical approaches are actually affordable for simulating turbulence-cascade interactions including serrated airfoils. The first one is relying on the Lattice–Boltzmann method, as proposed, for example, in [3], and that is also under study in the framework of InnoSTAT [4]. The second one discussed in the present paper is based on a hybrid computational fluid dynamics/computational aeroacoustics (CFD/CAA) method, involving a synthetic turbulence model. The first calculations performed on the InnoSTAT rectilinear cascade have already been reported in [5]. However, that study did not account for aerodynamic assessment of the serrated design, contrary to the present study. These simulations mainly focused on the determination of the best-suited numerical setup, in particular, depending on the number of vanes taken into account for the CAA. However, they were limited to one-dimensional and planar turbulence structures as inflow condition. The generation of a fully three-dimensional (3-D) turbulence structure investigated in this work still represents a challenging issue. Several methods have emerged to tackle this issue, such as the synthetic eddy method [6,7], extended to anisotropic flows and serrated airfoils [8,9], and the random particle mesh methodology [10] with recent developments to generate 3-D turbulence fields [11,12]. In this paper, the focus is put on synthetic turbulence modeling with a particular interest on the development and implementation of a fully three-dimensional vector field (with the complete three-wave numbers spectrum and three-velocity components). The tradeoff between the accuracy, central processing unit (CPU) time, and representativeness of the turbulence–airfoil interaction will be discussed throughout CAA simulations with one-dimensional (1-D), two-dimensional (2-D), and three-dimensional (3-D) turbulence fields injected at the entrance of the CAA domain. The method proposed here to generate synthetic turbulence structures is based on Fourier modes decomposition of the velocity introduced in [13–15]. Until now, it has been implemented at ONERA to correctly reproduce the upwash velocity component to the airfoil. That is the dominant component behind turbulence interaction noise mechanism, as shown, for example, analytically in [16] or through numerical simulations in [8] for serrated airfoils. The upwash velocity is represented via its autocorrelation spectrum and through planar turbulent structures. However, as shown in the present work, the latter approach is not directly expandable to 3-D turbulence structures. Consequently, the framework used for homogeneous isotropic turbulence generation and currently relying on the energy spectrum definition such as proposed in [14] and in [17] is considered. An equivalent mathematical formalism is originally proposed to still link the energy spectrum with wave number distribution over a spherical volume to the velocity autocorrelation spectra using Cartesian writing over a rectangular volume. This equivalence is drawn for both 2-D and 3-D turbulence structures. This paper follows on previous work on CAA with synthetic turbulence based on Fourier modes decomposition [1,2,18]. Turbulence-generation processes able to tackle some of the issues arising in simulations of practical configurations are implemented, such as wall and periodic boundary conditions (BC), while keeping the CPU time as low as possible. The new methodology is first validated and then applied on both baseline (untreated) and serrated (treated) geometries in the context of the InnoSTAT project. A comparison is performed with previous results and with semi-empirical and analytical solutions. A semi-empirical law proposed by Paruchuri et al. [19] is considered to link the power noise reduction to the Strouhal number St of single-wavelength serrations. Moreover, an analytical formulation to assess noise reductions provided by wavy leading edges has also been implemented, as detailed in [2]. It was initially developed at Cambridge University [20], by means of the Wiener–Hopf (WH) technique, and slightly extended and validated [2].

The structure of the paper is as follows. Section II describes the experimental setup at ECL. In Sec. III, the aeroacoustic numerical methodology used in this study is detailed. The development and implementation of synthetic turbulence-generation routines are summarized in Sec. IV. Issues raised by three-dimensional structures and associated with the boundary conditions of the CAA are highlighted. Sec. V presents CAA computations to assess noise emission on both baseline and serrated geometries. Finally, the aerodynamic performances evaluated by means of Reynolds-averaged Navier–Stokes (RANS) computations are discussed in Sec. VI.

II. Description of the Experimental Setup

The experimental facility (used for the first test campaign of the InnoSTAT project) consists of a rectilinear cascade, depicted in Figs. 1a and 1b, impinged by a roughly isotropic and homogeneous turbulence flow generated by an adequately shaped turbulence grid placed upstream of the airfoils inside the test section. Table 1 summarizes the main parameters expected to be representative of the approach condition at $M = 0.34$. In cases where two values are indicated, target values in parentheses indicate initial pretest values used for the present aeroacoustic calculations. As for the downstream far-field acoustic measurements, a microphone array will be placed at a distance $r = 1.88$ m from the cascade center, as illustrated in Fig. 1b. As for the instrumentation upstream, hot-wire anemometry at midspan will characterize the incoming turbulence, static pressure probes (transverse direction) will check the flow homogeneity, and an

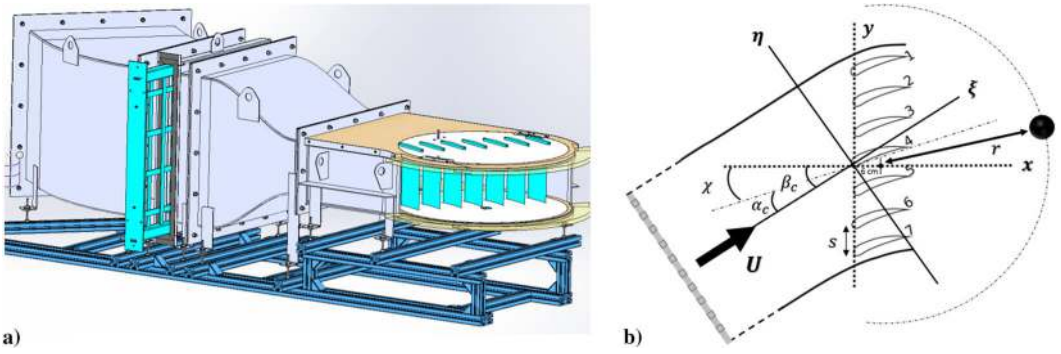

Fig. 1 Experimental facility: a) test facility for InnoSTAT at Ecole Centrale de Lyon and b) (x, y) cut of the geometry and coordinate systems.

Table 1 Main parameters of the rectilinear cascade configuration at approach condition (in parentheses, initial pretest values)

	Parameter	Value
Airfoil	Shape	NACA7310
	Chord c	12 cm
	Span L_z	20 cm
	Intervane space s	8.5 cm
Upstream flow	Mach number, $\boldsymbol{U}$ direction	0.34 (0.3)
	Entrance angle β_c	34 deg (30 deg)
Turbulence	Turbulence intensity (TI)	4.5% (5%)
	Turbulent length scale, $L_{\xi\xi}$	9 mm (8 mm)

axial microphone array will be used to separate waves propagating directions. In addition, probes will monitor the pressure at the airfoil skin.

III. Quick Overview of the Hybrid Computational Methodology

A hybrid method has been implemented at ONERA to conduct aeroacoustic studies, and a block diagram is provided in Fig. 2. The main step is the CAA simulation, achieved using the in-house code sAbrinA and solving the linearized Euler equations for perturbated variables, which are detailed in [21,22]. The unsteady flowfield is classically split in two parts, namely the mean flow $(\boldsymbol{U}, p_0, \rho_0)$, which has to be provided as an input, and the fluctuating part $(\boldsymbol{u}', p', \rho')$, which solution is computed by the code. Regarding numerical schemes, sAbrinA uses a sixth-order finite difference scheme for the spatial derivatives and a third-order multistage explicit Runge–Kutta scheme for the temporal discretization. Specific treatments and boundary conditions (BC) are implemented, such as a tenth-order filter in order to remove high-frequency oscillations and Tam and Dong boundary conditions [23], which are used to allow both the exit and entrance of the fluctuations in the domain without generating spurious noise sources or numerical reflections. The mean flow that advects the fluctuating variables is an input parameter of the CAA computations. A RANS computation is usually performed to this end. However, in order to comply with the nonviscous assumption of the CAA code, boundary layers have to be removed. To avoid this correction step, the mean flow has been obtained here by means of an open-source CFD code solving the Euler equations [24]. Turbulence inflow generated through a stochastic process is injected at the entrance of the CAA domain using Tam and Dong's nonreflective boundary condition. The procedure developed to obtain the synthetic turbulence is detailed in the next section. The third step is devoted to computation of sound radiation from an integral formulation. The fluctuating pressure p'_{wall} is extracted at the vane skin throughout simulation time and radiated to the far field using a Ffowcs Williams and Hawkings (FWH) [25,26] analogy with Green's function valid for a free-space medium with a uniform mean flow. The latter integral method is completed using the in-house code MIA.

IV. Synthetic Turbulence Modeling and Generation

A. Prescribed Geometry and Main Assumptions

The starting idea to synthesize turbulence is based on an ergodic stochastic process. First, a set average $\langle\rangle$ can be applied on the velocity field in order to get a decomposition in a mean part and a fluctuating part:

$$\begin{cases} \boldsymbol{u} = \boldsymbol{U} + \boldsymbol{u}' \\ \boldsymbol{U} = \langle \boldsymbol{u} \rangle \\ \langle \boldsymbol{u}' \rangle = 0 \end{cases} \tag{1}$$

For the configuration under study here, with almost a uniform mean flow, turbulence can be considered as being statistically steady. Hence,

$$\boldsymbol{u}'(\boldsymbol{X}, t) = \boldsymbol{u}'(\boldsymbol{X} + \boldsymbol{U}t_1, t + t_1), \quad \forall t_1$$

The validity of the frozen turbulence hypothesis depends on characteristic times of turbulence and of the advection by the mean flow. They must satisfy $\tau_{\text{turb}} \gg \tau_{\text{conv}}$, that is, $u'/U \ll 1$. The frozen turbulence assumption implies that the angular frequency of the velocity fluctuations is directly related to the wave vector, thanks to the following dispersion relation $\omega = \boldsymbol{k} \cdot \boldsymbol{U}$. In this study, the wave number spectra of turbulence are based on the definition given by Liepmann [27]:

$$E(k) = \frac{8\text{TI}^2 U^2 L_{\xi\xi}}{\pi} \frac{(kL_{\xi\xi})^4}{(1 + (kL_{\xi\xi})^2)^3} \quad \text{with} \quad k = \sqrt{k_\xi^2 + k_\eta^2 + k_z^2} \tag{2}$$

where the subscript $_\xi$ indicates the direction parallel to the mean flow, and TI, the turbulence intensity. From Eq. (2), the link with the autocorrelation velocity spectra can be made through [Eq. (9.1.8)] in [28]:

$$\varphi_{ii}^{3D}(k_\xi, k_\eta, k_z) = \frac{E(k)}{4\pi k^2}\left(1 - \frac{k_i^2}{k^2}\right) \tag{3}$$

In order to consider simplified cases with planar turbulence and also 1-D spectra, an integration is performed over transverse wave number components:

$$\varphi_{ii}^{2D}(k_\xi, k_z) = \int_{-\infty}^{+\infty} \varphi_{ii}^{3D}(k_\xi, k_\eta, k_z)\, \mathrm{d}k_\eta \tag{4}$$

$$\varphi_{ii}^{1D}(k_\xi) = \int_{-\infty}^{+\infty} \varphi_{ii}^{2D}(k_\xi, k_z)\, \mathrm{d}k_z \tag{5}$$

The previous integrations in Eqs. (4) and (5) can be analytically performed to obtain explicitly $\varphi_{\xi\xi}$, $\varphi_{\eta\eta}$, and φ_{zz}, which are of major interest for the implementation. They are listed in Table 2.

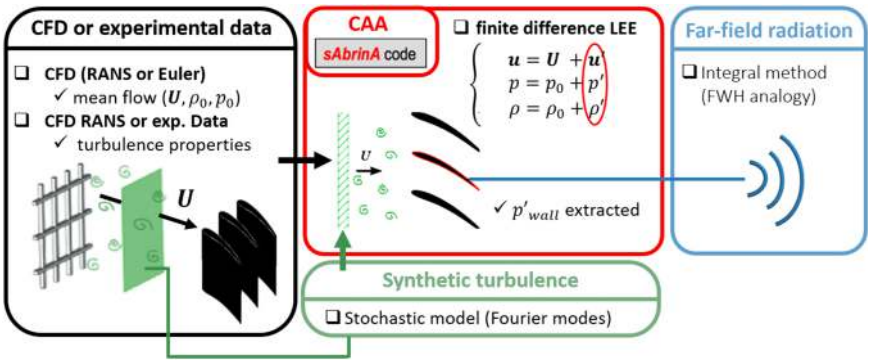

Fig. 2 Main components of the CFD/CAA computation chain.

Table 2 Integrated autocorrelation spectra obtained from Liepmann spectrum, Eq. (2)

2-D planar spectra $\varphi_{ii}^{2D}(k_\xi, k_z)$	1-D spectra $\varphi_{ii}^{1D}(k_\xi)$
$\varphi_{\xi\xi}^{2D}(k_\xi, k_z) = \frac{\mathrm{TI}^2U^2L_{\xi\xi}^2}{4\pi}\frac{1+L_{\xi\xi}^2(k_\xi^2+4k_z^2)}{(1+L_{\xi\xi}^2(k_\xi^2+k_z^2))^{5/2}}$	$\varphi_{\xi\xi}^{1D}(k_\xi) = \frac{\mathrm{TI}^2U^2L_{\xi\xi}}{\pi}\frac{1}{1+(L_{\xi\xi}k_\xi)^2}$
$\varphi_{\eta\eta}^{2D}(k_\xi, k_z) = \frac{3\mathrm{TI}^2U^2L_{\xi\xi}^4}{4\pi}\frac{k_\xi^2+k_z^2}{(1+L_{\xi\xi}^2(k_\xi^2+k_z^2))^{5/2}}$	$\varphi_{\eta\eta}^{1D}(k_\xi) = \frac{\mathrm{TI}^2U^2L_{\xi\xi}}{2\pi}\frac{1+3(L_{\xi\xi}k_\xi)^2}{(1+(L_{\xi\xi}k_\xi)^2)^2}$
$\varphi_{zz}^{2D}(k_\xi, k_z) = \frac{\mathrm{TI}^2U^2L_{\xi\xi}^2}{4\pi}\frac{1+L_{\xi\xi}^2(4k_\xi^2+k_z^2)}{(1+L_{\xi\xi}^2(k_\xi^2+k_z^2))^{5/2}}$	$\varphi_{zz}^{1D}(k_\xi) = \varphi_{\eta\eta}^{1D}(k_\xi)$

For simplified turbulence structures, one may choose not to consider the influence of the k_z component, with the subscript $_z$ referring to the direction aligned with the span of the studied airfoil or flat plate. Indeed, it has shown to be not significant for flat plates placed along the z axis, following Amiet theory under certain hypothesis (far-field observer located in the midspan plane) as detailed in [16,29]. Spectra are then not explicitly discretized along the latter direction since $k_z = 0$. To recover the expected magnitude of turbulence, a correction is required by multiplying the spectrum by a factor $\Delta k_z = 2\pi/L_z$, as proposed in [29]. Beyond these reminders of some assumptions commonly used in turbulence and aeroacoustic modeling, the particular geometrical characteristics and CAA setup of the rectilinear cascade facility, as depicted in Fig. 3, must be considered. First of all, in order to limit the CPU cost, the test facility is not fully included in the CAA. Adjacent vanes are taken into account through periodic boundary conditions applied along the y direction. Multichannel calculations can be performed, simply considering that $L_y = n_v s$. An example is given in Fig. 3 for $n_v = 1$. The cascade direction that is tilted from the normal axis to the mean flow, as shown by Fig. 1b, must be taken into account in the generation procedure since the gusts are injected in the coordinate system of the cascade (x, y, z) and not the one aligned with the mean flow (ξ, η, z). Therefore, to ensure periodicity, all wave numbers k_y have to be multiples of $2\pi/L_y$. Moreover, wall boundary conditions are taken into account for the CAA computations at both ends of the airfoil span. These slip flow boundary conditions considered for the CAA computations represent a major constraint for the generation of a fully 3-D turbulence, as explained later.

B. Computing Planar Turbulence Structures Through Velocity Autocorrelation Spectra

1. *Turbulence Structure* $(k_\xi, k_z = 0)$

First of all, let us consider the simplest turbulence field for 3-D geometries, namely, parallel gust, for which $k_y = 0$, as illustrated in Fig. 4. The divergence-free condition leads to the simple condition $\partial u_x'/\partial x = 0$. Thus, u_x' is constant (here zero), and the overall turbulence velocity is driven by the one-component velocity u_y'. To recover the prescribed normal velocity u_η', we set $u_y' = u_\eta'/\cos(\beta_c)$. The angular frequency is independent of the considered reference frame; therefore, $k_x = k_\xi/\cos(\beta_c) = \omega/U_x = \omega/(U\cos(\beta_c))$. The simplification $k_x x = k_\xi \xi$ comes from the fact that for the turbulence projections, a flat plate aligned with the mean flow is considered. All points of the flat plate being at a location $\eta = 0$, whereas, in the CAA, the airfoil thickness is considered. More details can be found in [22], pp. 132–134. The spatial discretization step is given by $\Delta k_{\xi,l} = \cos(\beta_c)\Delta k_{x,l}$, which can be associated with the angular frequency discretization through $\omega_l = 2\pi l \Delta f$. This equation allows to generate L modes equally distributed from $f_{\min} = \Delta f$ to $f_{\max} = L\Delta f$. For each mode l, a random phase ψ_l is also introduced. The autocorrelation spectrum of the upwash velocity component is defined by $\varphi_{\eta\eta}^{2D}(k_\xi, 0)$, referring to the $\varphi_{\eta\eta}^{2D}(k_\xi, k_z)$ definition in Table 2. Since the wave number k_z is set to zero, the turbulence spectrum has also to be weighted by $\Delta k_z = 2\pi/L_z$, in order to obtain the prescribed magnitude of the injected turbulence as mentioned in [29]:

$$u_y'(\boldsymbol{X}, t) = \frac{2}{\cos(\beta_c)}\sum_{l=1}^{L}\sqrt{\varphi_{\eta\eta}^{2D}(k_{\xi,l}, 0)\Delta k_\xi \frac{2\pi}{L_z}}\cos(k_{x,l}x - \omega_l t + \psi_l) \tag{6}$$

Since the synthetic turbulence [defined by Eq. (6)] depends only on the k_x wave number, the numerical results match exactly the analytical solution as depicted in Fig. 5.

2. *Turbulence Structure* (k_ξ, k_z)

For (k_ξ, k_z) turbulence, the same geometry and notations are used as previously, as illustrated by Fig. 3. The only difference is that the wave number k_z is no longer equal to zero. Instead, the wave numbers along the z direction are discretized following $k_{z,n} = n\Delta k_z$. Now, $L \times N$ angular phases ψ_{ln} are randomly selected. Figure 6 validates the good implementation of this spanwise varying turbulence:

$$u_y'(\boldsymbol{X}, t) = \frac{2}{\cos(\beta_c)}\sum_{l=1}^{L}\sum_{n=-N}^{N}\sqrt{\varphi_{\eta\eta}^{2D}(k_{\xi,l}, k_{z,n})\Delta k_\xi \Delta k_z} \times \cos(k_{x,l}x + k_{z,n}z - \omega_l t + \psi_{ln}) \tag{7}$$

even if the k_z variation gives rise to statistical errors in the power spectral density spectrum.

3. *Turbulence Structure* $(k_\xi, k_\eta, k_z = 0)$

The purpose of the structure $(k_\xi, k_\eta, 0)$ is to consider the pitchwise variations that should produce significant cascade effects in such rectilinear configurations. Figure 7 is helpful to follow the discussion. There are several ways to derive the equations for the injected velocities (u_x', u_y') or (u_ξ', u_η'), depending on the coordinate system. Two of them are listed as follows. Contrary to the (k_ξ, k_z) turbulence

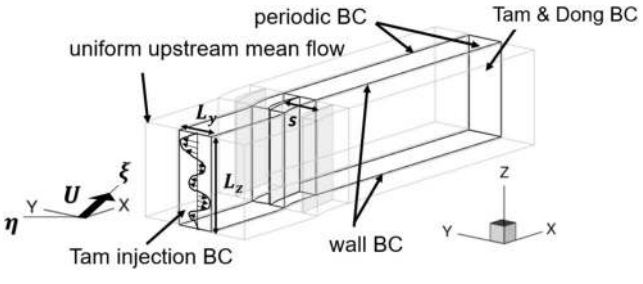

Fig. 3 Boundary conditions for the CAA computation.

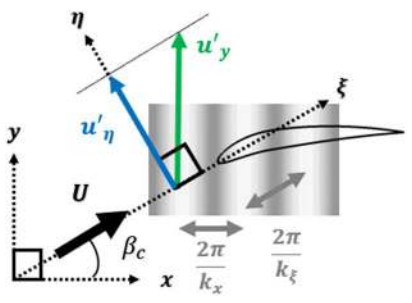

Fig. 4 Coordinate systems with associated wave numbers and involved turbulent velocities for turbulence structures lying in the plane k_ξ,k_z.

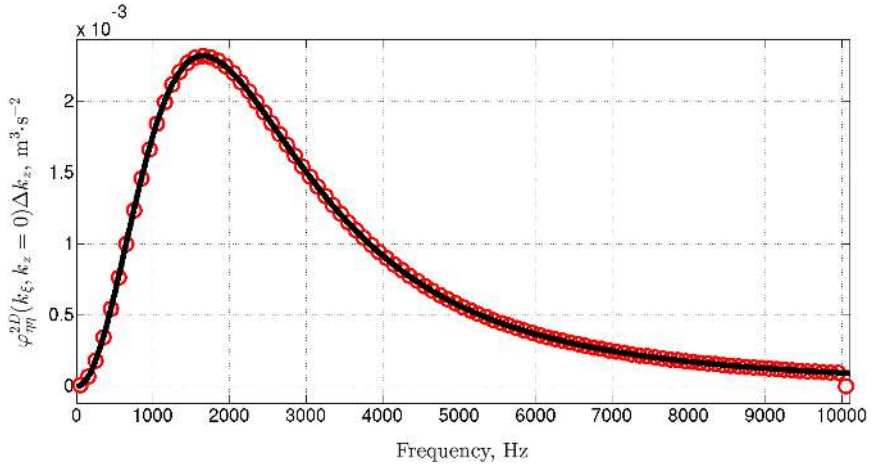

Fig. 5 Analytical spectrum of the upwash velocity component ——— and synthetic turbulence spectrum –○–, obtained with $\Delta f = 1$ Hz and averaged over 250 realizations.

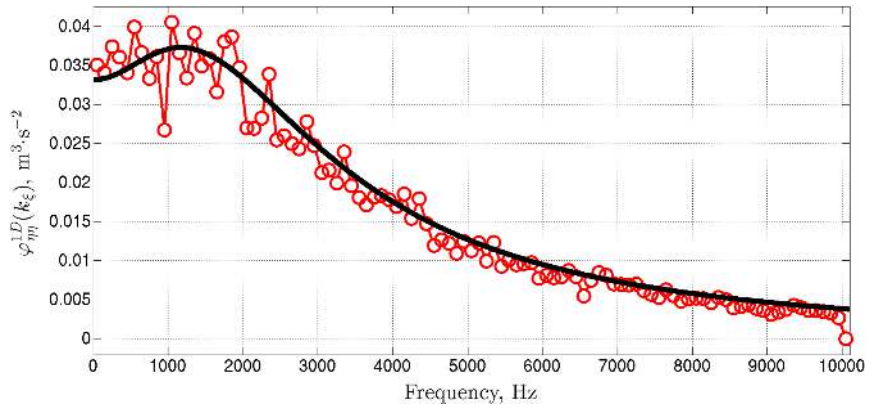

Fig. 6 Analytical spectrum of the upwash velocity component ——— and synthetic turbulence spectrum –○–, obtained with $N = 30$, $\Delta k_z = 2\pi/L_z$, $\Delta f = 1$ Hz, and averaged over 250 realizations.

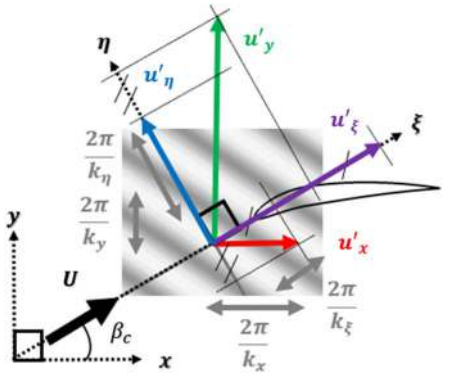

Fig. 7 Coordinate systems with associated wave numbers and involved turbulent velocities for turbulence structures lying in the plane k_ξ,k_η,$k_z = 0$.

for which the spectrum was integrated over k_η, the summation is explicitly defined here. Consequently, the u'_η component of the velocity is no more independent of the k_η wave number. To ensure a divergence-free solution, a second velocity component must be considered:

$$\frac{\partial u'_\xi}{\partial \xi} + \frac{\partial u'_\eta}{\partial \eta} = 0 \tag{8}$$

Consequently, u'_ξ is defined by $u'_\xi = -k_\eta/k_\xi u'_\eta$ and, furthermore, $\varphi^{3D}_{\xi\xi}(k_\xi, k_\eta, k_z = 0) = \varphi^{3D}_{\eta\eta}(k_\xi, k_\eta, k_z = 0)k_\eta^2/k_\xi^2$. The spectrum along the ξ axis is also correctly prescribed. Turbulence equations can also be obtained starting from the energy spectrum $E(k)$, as more usually considered in stochastic noise generation and radiation (SNGR) models [14]:

$$\boldsymbol{u}'(\boldsymbol{X}, t) = 2\sum_{k=1}^{K} \sqrt{E(k_k^\perp)\Delta k^\perp \frac{2\pi}{L_z}} \cos\left(\boldsymbol{k}_k^\perp \cdot \boldsymbol{X} - \omega_k t + \psi_k\right)\boldsymbol{\sigma}_k \tag{9}$$

where $k^\perp$ is defined such as $\boldsymbol{k}^\perp \cdot \boldsymbol{k}_z = 0$, $\omega_k = \boldsymbol{k}_k^\perp \cdot \boldsymbol{U}$, and $\boldsymbol{\sigma}$ is a unit vector such as $\boldsymbol{\sigma} \cdot \boldsymbol{k}^\perp = 0$. Equation (9) gives the discretized velocity for K modes distributed over a disk. As for $(k_\xi, k_z = 0)$ turbulence, a factor $2\pi/L_z$ has to be taken into account to recover the expected magnitude of the spectra. However, here, the turbulence modes are mapped on a rectangular box in the wave number space. This discretization proposed by Gill et al. [15] represents an original variant to the classical SNGR formulation [14,17]. The wave number relations are $k_{\xi,l} = 2\pi l \Delta f/U = \cos(\beta_c)k_{x,lm} + \sin(\beta_c)k_{y,m}$ and $k_{\eta,lm} = -\sin(\beta_c)k_{x,lm} + \cos(\beta_c)k_{y,m}$:

$$\boldsymbol{u}'(\boldsymbol{X}, t) = 2\sum_{l=1}^{L}\sum_{m=-M}^{M} \sqrt{\frac{E\left(\sqrt{k_{\xi,l}^2 + k_{\eta,lm}^2}\right)}{\pi k^\perp}\Delta k_\xi \Delta k_\eta \frac{2\pi}{L_z}} \times \cos\left(k_{\xi,l}\xi + k_{\eta,lm}\eta - \omega_l t + \psi_{lm}\right)\boldsymbol{\sigma}_{\mathrm{lm}} \tag{10}$$

A similar equation is provided by Gea-Aguilera et al. [7]. The wave number decomposition along the spatial directions in Eq. (10) easily ensures the periodic boundary condition along the y direction by satisfying $k_{y,m} = \boldsymbol{k}^\perp \cdot \boldsymbol{y} = m2\pi/L_y$, with m an integer. The

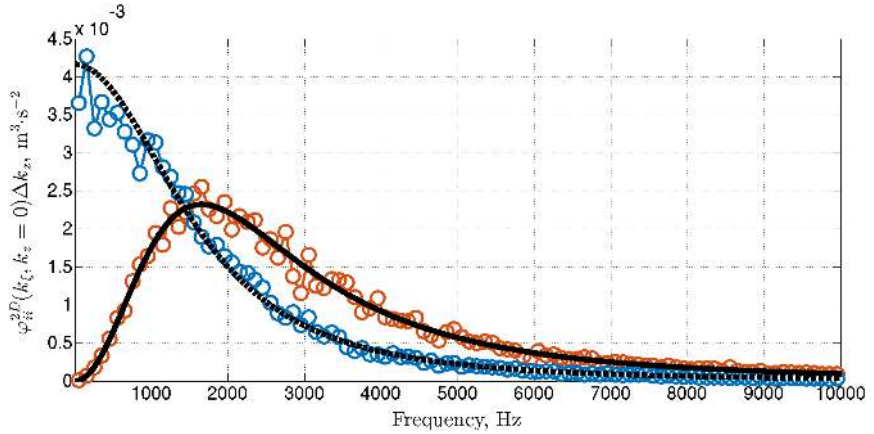

Fig. 8 Analytical upwash ——— and streamwise ····· spectra. Synthetic upwash –○– and streamwise –○– spectra, with $M = 16$, $L_y = s = 8.5$ cm, $\Delta f = 1$ Hz, and averaged over 250 realizations.

formulation coming from the autocorrelation velocity spectra can be recovered considering that $E(k^{\perp}) = \varphi^{3D}_{\eta\eta}(k_\xi, k_\eta, 0)4\pi k^{4\perp}/k_\xi^2$, $E(k^{\perp}) = \varphi^{3D}_{\xi\xi}(k_\xi, k_\eta, 0)4\pi k^{4\perp}/k_\eta^2$, and $\sigma_{\xi,lm} = \pm k_{\eta,lm}/k^{\perp}, \sigma_{\eta,lm} = \pm k_{\xi,l}/k^{\perp}$. The gusts are then generated as follows:

$$u'_\xi(\boldsymbol{X},t) = -2\sum_{l=1}^{L}\sum_{m=-M}^{M}\frac{k_\eta}{k_\xi}\sqrt{\varphi^{3D}_{\eta\eta}(k_{\xi,l},k_{\eta,lm},0)\Delta k_\xi \Delta k_\eta \frac{2\pi}{L_z}} \times \cos(k_{\xi,l}\xi + k_{\eta,lm}\eta - \omega_l t + \psi_{lm})$$

$$u'_\eta(\boldsymbol{X},t) = 2\sum_{l=1}^{L}\sum_{m=-M}^{M}\sqrt{\varphi^{3D}_{\eta\eta}(k_{\xi,l},k_{\eta,lm},0)\Delta k_\xi \Delta k_\eta \frac{2\pi}{L_z}} \times \cos(k_{\xi,l}\xi + k_{\eta,lm}\eta - \omega_l t + \psi_{lm}) \quad (11)$$

Moreover, the wave numbers in the upstream mean flow frame can be expressed as $k_{\xi,l} = \cos(\beta_c)k_{x,lm} + \sin(\beta_c)k_{y,m}$ and $k_{\eta,lm} = -\sin(\beta_c)k_{x,lm} + \cos(\beta_c)k_{y,m}$, which can be deduced from Fig. 7. The numerical implementation is validated for both streamwise and upwash velocity components as plotted in Fig. 8.

C. Framework for Generating Fully 3-D Turbulence Structures

1. Choice of an Adapted Energy Spectrum Description and Equivalence with Autocorrelation Formulations

Let us see now how to obtain a fully three-wave number spectrum. The role of all the wave number components on the aeroacoustic response can thus be investigated for both the impinged baseline and serrated airfoils in a cascade configuration. As a preliminary step, it can be useful to underline the failure of a turbulent field built with only two components ($u'_\xi(k_\xi, k_\eta, k_z)$ and $u'_\eta(k_\xi, k_\eta, k_z)$), with

$$u'_\eta(\boldsymbol{X},t) = 2\sum_{l=1}^{L}\sum_{m=-M}^{M}\sum_{n=-N}^{N}\sqrt{\varphi^{3D}_{\eta\eta}(k_{\xi,l},k_{\eta,lm},k_{z,n})\Delta k_\xi \Delta k_\eta \Delta k_z} \times \cos(k_{\xi,l}\xi + k_{\eta,lm}\eta + k_{z,n}z - \omega_l t + \psi_{\mathrm{lmn}})$$

$$u'_\xi(\boldsymbol{X},t) = -2\sum_{l=1}^{L}\sum_{m=-M}^{M}\sum_{n=-N}^{N}\frac{k_{\eta,lm}}{k_{\xi,l}}\sqrt{\varphi^{3D}_{\eta\eta}(k_{\xi,l},k_{\eta,lm},k_{z,n})\Delta k_\xi \Delta k_\eta \Delta k_z} \times \cos(k_{\xi,l}\xi + k_{\eta,lm}\eta + k_{z,n}z - \omega_l t + \psi_{\mathrm{lmn}}) \quad (12)$$

The autocorrelation spectrum of the u'_ξ component where the summation over the k_η wave number has been replaced by an integral is considered:

$$\varphi^{2D}_{\mathrm{pseudo},\xi\xi}(k_\xi, k_z) = \frac{\mathrm{TI}^2 U^2 L^2_{\xi\xi}}{4\pi}\frac{1}{k_\xi^2}\frac{(k_\xi^2 + k_z^2)}{(1 + L^2_{\xi\xi}(k_\xi^2 + k_z^2))^{3/2}} \quad (13)$$

After integration, Eq. (13) is providing a so-called pseudo 2-D autocorrelation spectrum. The 1-D spectrum should be obtained from an integration over k_z. However, this $\varphi^{2D}_{\mathrm{pseudo},\xi\xi}(k_\xi, k_z)$ tends asymptotically to $1/|k_z|$, which prevents the convergence of the integral with respect to k_z. Moreover, close to low frequencies, the solution will diverge due to the $1/k_\xi^2$ term. That is why, even if in practice u'_ξ is discretized over finite intervals and not over $\mathbb{R}^2$, this formulation leads to very high values of the velocity component along the ξ axis. For a flat plate impacted by such gusts, u'_ξ plays absolutely any role and there is thus no issue. However, for a NACA airfoil with a nonzero thickness, an issue may appear if the magnitude of u'_ξ is much higher in comparison with what it should be if turbulence had been properly defined. Consequently, the generated gusts have to include a nonzero component u'_z in order to match correctly the three components of the autocorrelation spectra.

Each velocity component is now defined through its spectral tensor following Eq. (3), with

$$u'_i(\boldsymbol{X},t) = 2\sum_{l=1}^{L}\sum_{m=-M}^{M}\sum_{n=-N}^{N}\sqrt{\varphi^{3D}_{ii}(k_{\xi,l},k_{\eta,lm},k_{z,n})\Delta k_\xi \Delta k_\eta \Delta k_z} \times \cos(k_{\xi,l}\xi + k_{\eta,lm}\eta + k_{z,n}z - \omega_l t + \psi_{\mathrm{lmn}}) \quad (14)$$

The turbulent field must satisfy the incompressibility condition in order to avoid the creation of spurious sources, which leads to

$$\frac{\partial u'_x}{\partial x} + \frac{\partial u'_y}{\partial y} + \frac{\partial u'_z}{\partial z} = 0 \Leftrightarrow \sum_i k_i\sqrt{\varphi^{3D}_{ii}} = 0 \quad (15)$$

When injecting $\varphi^{3D}_{\xi\xi}$ and $\varphi^{3D}_{\eta\eta}$ in Eq. (15), one can deduce that φ^{3D}_{zz} is inadequately prescribed. Namely,

$$\varphi^{3D}_{\mathrm{pseudo},zz}(k_\xi,k_\eta,k_z) = \frac{1}{k_z^2}\frac{\left(k_\xi\sqrt{k_\eta^2+k_z^2} + k_\eta\sqrt{k_\xi^2+k_z^2}\right)^2}{k_\xi^2+k_\eta^2}\varphi^{3D}_{zz}(k_\xi,k_\eta,k_z) \quad (16)$$

The shape of the spectrum is strongly altered. Although the component $\varphi_{\eta\eta}$ plays a key role in the aeroacoustic response [8], nonnegligible effects might be expected. For this reason, the most reasonable path to obtain a fully 3-D turbulence relies again on the usual SNGR formalism already initiated with $(k_\xi, k_\eta, k_z = 0)$ turbulence:

$$\boldsymbol{u}'(\boldsymbol{X},t) = 2\sum_{k=1}^{K}\sqrt{E(k_k)\Delta k}\cos(\boldsymbol{k_k}\cdot\boldsymbol{X} - \omega_l t + \psi_k)\boldsymbol{\sigma_k} \quad (17)$$

Equation (17) is the general form of Eq. (9). However, it is not possible to take directly into account the periodic boundary conditions in the y direction $k_y = m2\pi/L_y$. The present approach generalizes the key idea already probed with the $(k_\xi, k_\eta, 0)$ turbulence

structure. The wave number space is no more discretized by spherical volumes of an equivalent radius k and thickness Δk but by rectangular boxes with an elementary volume $\Delta k_\xi \Delta k_\eta \Delta k_z$. The relation between the two discretizations is given by $\Delta k \cong \Delta k_\xi \Delta k_\eta \Delta k_z / (2\pi k^2)$, and the velocity field is expressed as

$$\boldsymbol{u}'(\boldsymbol{X},t) = 2\sum_{l=1}^{L}\sum_{m=-M}^{M}\sum_{n=-N}^{N}\sqrt{\frac{E\left(\sqrt{k_{\xi,l}^2+k_{\eta,lm}^2+k_{z,n}^2}\right)}{2\pi k^2}\Delta k_\xi \Delta k_\eta \Delta k_z} \times \cos(k_{\xi,l}\xi + k_{\eta,lm}\eta + k_{z,n}z - \omega_l t + \psi_{\mathrm{lmn}})\boldsymbol{\sigma}_{\mathrm{lmn}} \tag{18}$$

A similar decomposition has been proposed by Gill et al. [15]. The divergence-free condition is now given by $\boldsymbol{k}\cdot\boldsymbol{\sigma}_{\mathrm{lmn}} = 0$, with $\boldsymbol{k} = (k_{\xi,l}, k_{\eta,lm}, k_{z,n})^T$ and $\boldsymbol{\sigma}_{\mathrm{lmn}}$, a unit vector. The direction of the turbulent velocity in Eq. (18) has to be determined. This is practically achieved by means of an efficient algorithm, similarly to [14], whose main steps are summarized in Appendix A. In Appendix B, a piece of demonstration is given to show the consistency between this modified energy spectrum formalism proposed here and previous formulations.

2. Taking into Account Wall-Boundary Conditions by Means of a Nondivergence-Free Window Function

The full 3-D turbulence formulation implies that a vertical velocity component u_z' has to be considered. This additional component must be damped near the wall boundaries in order to avoid spurious noise sources, which is a nontrivial issue. A window function $f_w(z)$ is applied to a stochastic velocity field, defined here for a single wave vector component in order to simplify the notations

$$\boldsymbol{u}'(\boldsymbol{X},t) = A f_w(z)\cos(\boldsymbol{k}\cdot\boldsymbol{X} - \omega t + \psi)\boldsymbol{\sigma} \tag{19}$$

where A is the initial amplitude of this given fluctuation, such as the velocity tends to zero near the wall boundaries. The chosen windowing, without care on divergence, is a gate function with half-sinusoidal lobes on each side controlled by a length size L_w:

$$\begin{cases} \forall\, z \in [z_{\min}, z_{\min}+L_w], & f_w(z) = \dfrac{1}{2}\left(1-\cos\left(\pi\dfrac{z-z_{\min}}{L_w}\right)\right) \quad \text{and} \quad f_w'(z) = \dfrac{\pi}{2L_w}\sin\left(\pi\dfrac{z-z_{\min}}{L_w}\right) \\ \forall\, z \in [z_{\min}+L_w, z_{\max}-L_w], & f_w(z) = 1 \quad \text{and} \quad f_w'(z) = 0 \\ \forall\, z \in [z_{\max}-L_w, z_{\max}], & f_w(z) = \dfrac{1}{2}\left(1+\cos\left(\pi\dfrac{z-(z_{\max}-L_w)}{L_w}\right)\right) \quad \text{and} \quad f_w'(z) = -\dfrac{\pi}{2L_w}\sin\left(\pi\dfrac{z-(z_{\max}-L_w)}{L_w}\right) \end{cases} \tag{20}$$

The function f_w proposed in Eq. (20) ensures a smooth, that is, without discontinuity, transition to the zero velocity condition at wall boundaries due to the fact that f_w is C^1 (differentiable function whose derivative is continuous) everywhere on the interval $[z_{\min}, z_{\max}]$ and that $f_w(z_{\min}) = f_w(z_{\max}) = f_w'(z_{\min}) = f_w'(z_{\max}) = 0$:

$$\mathrm{div}(\boldsymbol{u}') = f_w'(z)A\cos(\boldsymbol{k}\cdot\boldsymbol{X} - \omega t + \psi)\sigma_z \neq 0 \tag{21}$$

The divergence-free property of the synthetic turbulence field is no more ensured when the windowing is introduced. The impact on the far-field acoustics will be discussed on the baseline numerical simulations in Sec. V.

An example of a window function is presented in Fig. 9. Figures 10a and 10b show, respectively, turbulence spectra at $z = 0$ (where $f_w(z) = 1$) and $z = 0.185$ (where $f_w(z) = 0.5$). They demonstrate a good agreement with the theoretical spectra, which validates the adapted formulation relying on the energy spectrum. Since the windowing consists simply in the multiplication of the turbulence fluctuations by a constant, the spectra amplitude at $z = 0.185$ are simply reduced here by a factor 0.5^2 as illustrated in Fig. 10b.

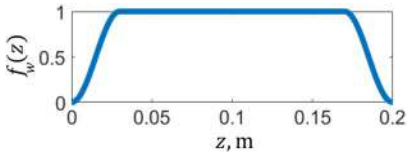

Fig. 9 $f_w(z)$ with $R_w = L_w/L_z = 15\%$ and $L_z = 0.2$ m.

3. Theoretical Development and Implementation of a Divergence-Free Windowed Field

The choice has been made to only modify the component u_z' in Eq. (21) since it plays a minor role in the noise source generation process:

$$\frac{\partial u_z'}{\partial z} = -f_w(z)A\sin(\boldsymbol{k}\cdot\boldsymbol{X} - \omega t + \psi)k_z\sigma_z + f_w'(z)A\cos(\boldsymbol{k}\cdot\boldsymbol{X} - \omega t + \psi)\sigma_z - g_w'(z)A\sigma_z \tag{22}$$

Consequently, in order to cancel the additional spurious term in Eq. (21), the derivative of u_z' is modified by means of a corrective function $g_w(z)$, as shown in in Eq. (22). Other options would have been to alter all the components of the velocity. However, it would have led to less accurate acoustic predictions, especially since the spectrum of the perpendicular component to the airfoils u_η would have been modified. Another option could have consisted in shifting phases to obtain a zero velocity at walls. However, it would have led to a complete loss of the spatial correlation (and representativeness of turbulence length scales) along the spanwise direction. The spatial correlation plays a major role regarding the noise reduction mechanism obtained with a serrated design.

After some calculations ensuring $(f_w, g_w) \in C^1$ and boundary conditions refer to Eq. (C8) in Appendix C, one can show that the following equality must be satisfied:

$$\begin{cases} g_w(z_{\min}) = g_w(z_{\max}) = 0 \\ g_w(z_{\min}+L_w) = g_w(z_{\max}-L_w) \end{cases} \Rightarrow \cos\left(k_x x + k_y y + k_z z_{\min} + \frac{k_z L_w}{2} - \omega t + \psi\right)\cos\left(\frac{k_z L_w}{2}\right) = \cos\left(k_x x + k_y y + k_z z_{\min} + k_z L_z - \frac{k_z L_w}{2} - \omega t + \psi\right)\cos\left(\frac{k_z L_w}{2}\right) \tag{23}$$

There are two types of constraints that can be applied on k_z to ensure the equality coming from Eq. (23). Firstly, let us consider that $\cos(k_z L_\omega/2) = 0$, satisfying Eq. (23), which gives $0 = 0$. Under this assumption, $k_z = (2n+1)\pi/L_w$ with $n \in \mathbb{N}$. However, since $k_z \neq \pi/L_w$ (see Appendix C), this solution implies that the discretization cannot be uniformly spaced, since one cannot chose whatever integer $n \in \mathbb{N}$. Moreover, if L_w is chosen too small, the discretization steps tends to become very wide, which could affect the precision of

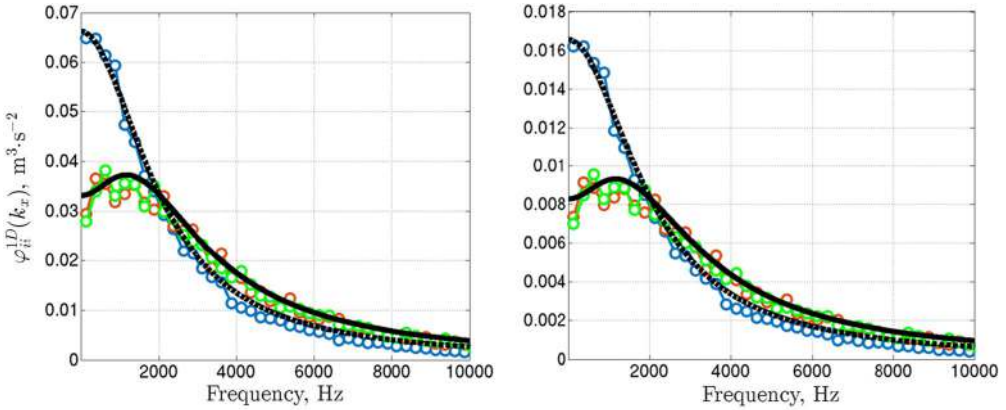

a) Spectra at location $z = 0.1$ where $f_w(z) = 1.0$ **b) Spectra at location $z = 0.185$ where $f_w(z) = 0.5$**

Fig. 10 Analytical upwash, spanwise ——— and streamwise ····· spectra. Synthetic upwash –○–, spanwise –○–, and streamwise –○– spectra, with $N = 30$, $R_w = 15\%$, $M = 16$, $L_y = s = 8.5$ cm, $\Delta f = 1$ Hz, and averaged over 250 realizations.

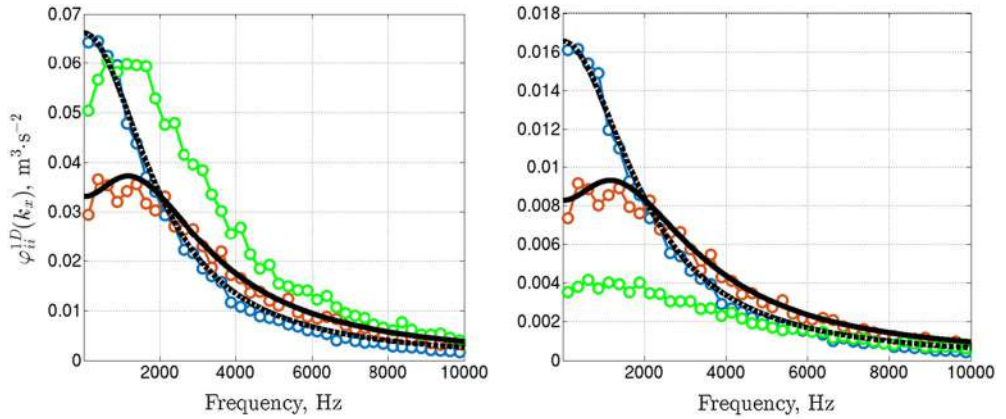

a) Spectra at location $z = 0.1$ where $f_w(z) = 1.0$ **b) Spectra at location $z = 0.185$ where $f_w(z) = 0.5$**

Fig. 11 Analytical upwash, spanwise ——— and streamwise ····· spectra. Synthetic upwash –○–, spanwise –○–, and streamwise –○– spectra, with $N = 30$, $R_w = 15\%$, $M = 16$, $L_y = s = 8.5$ cm, $\Delta f = 1$ Hz, and averaged over 250 realizations.

the solution. Another possibility is to consider $k_z = 2n\pi/(L_z - L_w)$, for which the left-hand side and right-hand side of Eq. (23) become $\cos(k_x x + k_y y + 2n\pi(z_{\min} + L_w/2)/(L_z - L_w) - \omega t + \psi)\cos(2n\pi L_w/(2L_z - 2L_w))$. The case $R_w = 15\%$ provides the same envelope as that for the nondivergence-free scenario, but with a slightly shifted discretization of the k_z wave numbers, $2n\pi/(L_z - L_w)$ instead of $2n\pi/L_z$. The generated spectra with the new implementation are compared with the analytical solutions in Figs. 11a and 11b. There is a good agreement for the streamwise and upwash components for all cases. The fact that the spanwise spectra are altered is related to the choice of applying the correction on the u_z' component of the velocity.

4. *Numerical Optimization*

The synthetic turbulence-generation process has been implemented in FORTRAN code. Previous routines used at ONERA for annular geometries [1,2] have been rewritten in a Cartesian coordinate system. In parallel, several features have been added in order to lower the CPU generation cost. Turbulence structures having a symmetry axis are generated only on a line of the mesh and duplicated afterwards on all the injection planes. Turbulence equations have been decomposed as much as possible using trigonometric identities to factorize operations. In order to speed up the generation process of a fully 3-D synthetic turbulence, some additional optimization has been needed. It has been chosen not to generate turbulence over all the time steps of the simulation, similarly to [11]. The missing time steps are recovered by a linear interpolation. For example, here, the synthetic turbulence field has been generated one time step over 10 on the baseline computations, still ensuring 40 points per period at the highest simulated frequency. For each three-channel simulation presented in the following, the 3-D turbulence-generation process has required only around 10 h on one thousand cores, for which the CAA converged solution was obtained in about 30 h on 1077 cores on the baseline geometry. The ratio between the CPU time dedicated to the turbulence generation and CAA simulations is presented in Table 3 for various turbulent fields. The generation time is negligible for one-dimensionnal and planar turbulent structures. However, if the fully 3-D turbulence had been generated over all time steps it would have represented almost four times the CAA cost (around 2500 h on 100 cores). The 3-D turbulence field is instead generated on sampled time steps without altering the quality of the solution since the characteristic time of the turbulence is much higher than the time step of the CAA calculation.

A flow chart representing the 3-D turbulence generation has also been added in Appendix D.

Table 3 Comparison of CPU times for turbulence generation and CAA calculations

3-channel computations (on the serrated geometry)	Generation time of turbulence (on 100 cores)	Ratio with respect to CAA time (with $T_{\text{simulation}} = 3\Delta f$)
$k_\xi, k_z = 0$	≈20 min	<0.1%
k_ξ, k_z	≈40 min	≈0.1%
$k_\xi, k_\eta, k_z = 0$	≈2 h	≈0.3%
k_ξ, k_η, k_z (with interpolation)	≈100 h	≈15%

V. Aeroacoustic Applications on the Rectilinear Cascade Configuration

A. Introduction to the Numerical Setup on the Baseline Geometry

1. *Inviscid Mean Flow Calculation*

The mean flow has been computed by means of a 2-D open-source Euler code proposed in [24]. Inflow conditions are indicated in Fig. 12. A few loops have been performed to get the targeted upstream Mach number of 0.3. This has been done by adjusting the exhaust static pressure. This approach was shown to be an efficient alternative to the previous RANS approach, which requires some corrections near the solid boundaries in order to remove boundary layers and recirculation zones, incompatible with the inviscid assumption of the CAA code. For the mean flow computation, a single channel simulation with periodic boundary condition has been considered. The obtained mean velocity field has been then duplicated and interpolated on the CAA mesh for acoustic multichannel computations. The upstream Mach number and the entrance flow angle used for the CAA were chosen before the final values, corresponding to the pretest values in Table 1. It should not modify the conclusions drawn here.

2. *Simulated Configuration and Main Assumptions of the Aeroacoustic Computations*

The CAA simulation setup uses the boundary conditions presented in Figs. 3 and 12. Except for the one-channel computations and the parametric study on the vane count from [5] on the baseline geometry, which are performed on an H pattern grid [5], the whole CAA grid is designed using an O-H pattern. This choice facilitates the generation of the 3-D mesh for the serrated geometry. Indeed, the mesh is practically designed using an in-house tool, ersatZ, which allows to apply suitable 3-D deformations on the reference skeleton to obtain the serrated shape and to extend them within the grid volume [5]. The main conclusion from this preliminary study was that multichannel computations are mandatory to avoid spurious resonance phenomena in the midfrequency range resulting from periodic boundary conditions and requiring to include at least three-vane channels in the CAA domain. A typical result from these parametric studies [5] is shown in Fig. 13. All the simulations discussed in the next paragraphs are carried out using three-vane channels, and first solutions from [5] are completed using fully 3-D turbulence modeling.

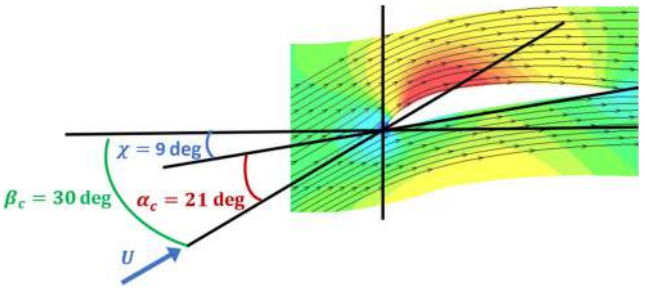

Fig. 12 U_x, levels between 60 and 120 m · s^{-1}.

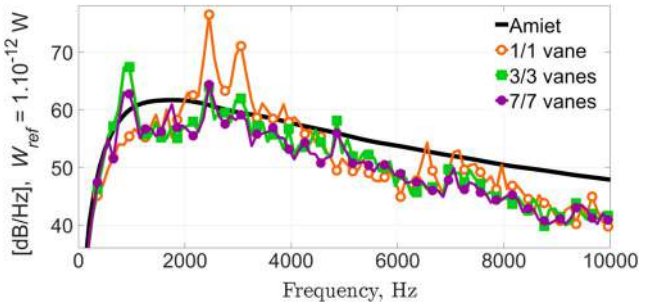

Fig. 13 Downstream sound power per vane from [5], with a $k_\xi, k_\eta, k_z = 0$ turbulence. Computations performed with $\Delta f = 10$ Hz and averaged over 10 realizations.

B. Aeroacoustic Predictions on the Baseline (Untreated) Geometry

The parameters used for the generation of the 3-D synthetic turbulence are the following: $L_y = 0.255$ m, $M = 48$, $N = 30$, and $\Delta f = 100$ Hz. In Fig. 14, snapshots of synthetic turbulent flows related to the transverse velocity u'_y are clearly showing the different patterns issued from 1-D (Fig. 14a), 2-D (Figs. 14b and 14c), and 3-D (Fig. 14d) injected turbulence. Note that 1-D (parallel gust), 2-D (planar), and fully 3-D structures are, respectively, linked to the number of velocity components (1, 2, or 3) [15] and then to the nonzero wave numbers involved in the present turbulence models.

The pressure fluctuations are then extracted at the vane skin and radiated in the far field using an in-house code called MIA. MIA solves the FWH equation restricted here to the loading noise term with a solid surface formulation. The power spectra were obtained by a weighted angular integral over half a circle downstream of the cascade, as performed in [5]. In order to compensate for the lack of energy input due to the window function $f_w(z)$, with $R_w = 0.15$, a simple correction $20\log(1/(1 - R_w))$ has been applied to the spectra. The numerical spectra are compared to Amiet's solution for an isolated flat plate in Fig. 15. Please note that a cascade model as proposed in [30–32] might be used to get a reliable reference solution, so that the Amiet-based spectrum is only giving a biased estimate by neglecting the cascade effect (quite significant in this configuration). At high frequencies, Amiet's model is overpredicting the acoustic spectra because it does not take into account any thickness. For $(k_\xi, k_z = 0)$, (k_ξ, k_z), and (k_ξ, k_η, k_z) turbulent structures, the computations have been performed with $\Delta f = 100$ Hz and with $\Delta f = 20$ Hz for $(k_\xi, k_\eta, k_z = 0)$ turbulence.

Regarding the numerical spectra associated with $(k_\xi, k_z = 0)$ and $(k_\xi, k_\eta, k_z = 0)$ turbulence, one may notice that taking into account k_η provides a more constant slope at medium- and high-frequency range. However, the bump (around 800 Hz) due to a numerical amplification using periodicity conditions over three-vane channels instead of seven is stronger when a turbulence with a varying k_η is injected; see Fig. 15 from [5]. Regarding the comparison between CAA results and Amiet's solution, the levels are definitely overestimated by the isolated flat plate approximation. This is why, even if the nonzero divergence turbulence is the closest solution to one from Amiet, it represents in fact the worst numerical prediction. Indeed, following literature [32,33], a few decibels' reduction is at least expected at low frequencies due to the cascade effect and at high frequencies due to the nonzero thickness of the airfoils [34]. Looking at the divergence-free result, taking into account the k_z wave number

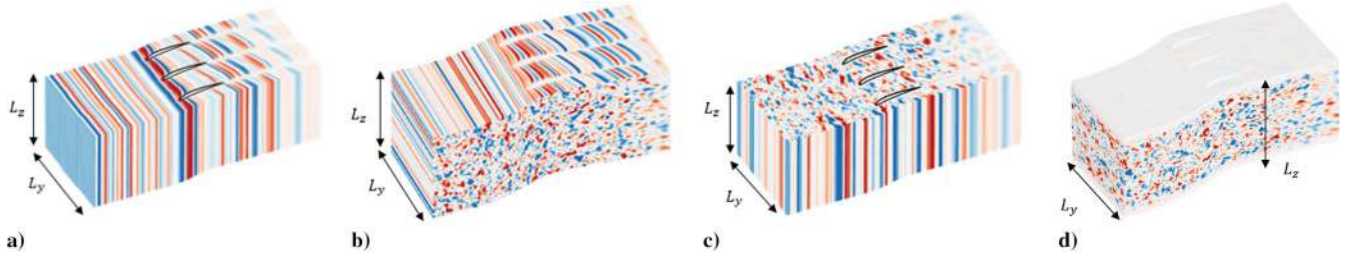

Fig. 14 Turbulent-like u'_y snapshots (levels between ±2 m · s^{-1} for the $k_z = 0$ cases and ±10 m · s^{-1} otherwise). Turbulence structures a) $k_\xi, k_z = 0$, b) k_ξ, k_z, c) $k_\xi, k_\eta, k_z = 0$, and d) k_ξ, k_η, k_z.

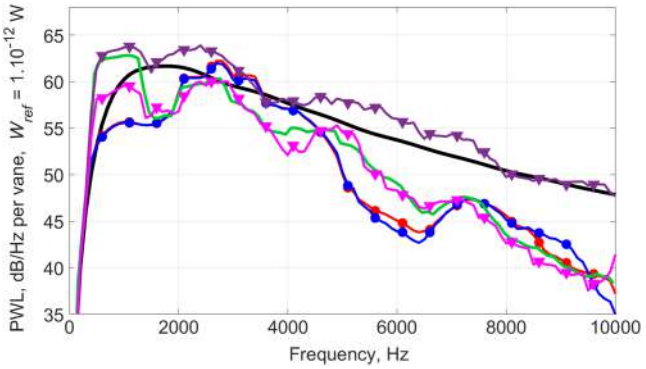

Fig. 15 Amiet's solution ——. Numerical spectra with a 1 kHz moving average: $k_\xi, k_z = 0$ —●—, k_ξ, k_z —●—, $k_\xi, k_\eta, k_z = 0$ ——, k_ξ, k_η, k_z with $\mathrm{div}(u') \neq 0$ —▼—, and k_ξ, k_η, k_z with $\mathrm{div}(u') = 0$ —▼—.

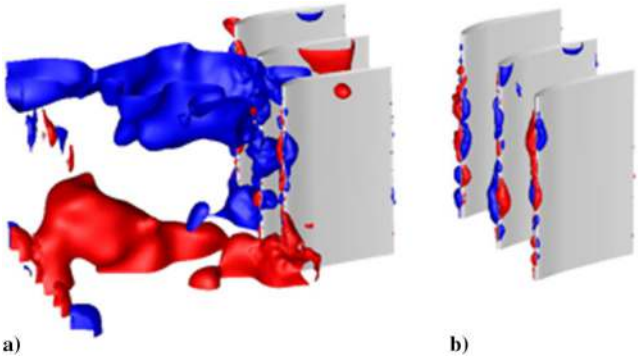

Fig. 17 Isosurfaces of p' at ±200 Pa. Turbulence k_ξ, k_η, k_z with a) nonzero divergence and k_ξ, k_η, k_z with b) divergence-free formulation.

seems not to modify the spectra (green vs pink curves) except for the resonance bump at low frequencies (link with the three-channel periodicity), which is in accordance with previous numerical simulations [5] and with Amiet's theory.

Snapshots of the turbulent-like velocity divergence are plotted in Fig. 16, at the injection plane. In the nonzero divergence case plotted in Fig. 16a, divergence is nonnegligible in the region where the window function derivative is maximum. On the contrary, with the divergence-free formulation, the issue disappears as illustrated in Fig. 16b. As clearly visible on isosurfaces of fluctuating pressure in Fig. 17, the nonzero divergence formulations (Fig. 17a) give rise, close to areas of maximum divergence in Fig. 16a, to local intense spots extending through the CAA domain and interacting with the vanes and responsible for some noise increase. On the contrary, the solution obtained with the divergence-free formulation (Fig. 17b) is found to be much cleaner without generation of additional spurious numerical sources.

C. Design of a Passive Treatment Based on Leading-Edge Serrations

The leading-edge serrations have been firstly designed on a 2-D plane, plotted in Fig. 18a, following the background from previous studies; the most recent is presented in [2]. The theoretical optimal serration wavelength, defined from [19], corresponds to twice the turbulence length scale of 8 mm. The serration amplitude is defined directly related to the serration angle and so the ratio h_s/λ_s. Although the acoustic benefit could be improved by increasing h_s, a practical limitation of the ratio h_s/c is required to avoid a noticeable loss of aerodynamic performance for industrial applications. Such a threshold has been used in [2]. Hence, setting $h_s/\lambda_s = 1$ can be considered as a reasonable value close to the optimum design. For the numerical computation, in order to get an integer number of serrations along the span, the quantities have been slightly increased to end with $h_s = \lambda_s = 16.7$ mm. To apply the planar deformation on the 3-D geometry of the airfoil, the ersatZ tool has been used. The first step has consisted in the extraction of the camber and thickness laws. A homothety has been then applied to these laws in order to obtain the shape of the airfoil at the roots of the serrations. To get the airfoil geometry at the hills of the serrations, the camber law was extended at the leading edge, keeping a constant angle as illustrated in Fig. 18b. The ersatZ modeler, which is able to extend the skeleton deformations (see Fig. 18c) to the cells of the volume mesh, has been used to apply a morphing of the baseline CAA grid, presented in Fig. 19, in order to perform aeroacoustic simulations on the low-noise design.

D. Assessment of the Noise Reduction Provided by the Serrated Geometry

1. *Mean Flow and CAA Computation*

In order to obtain the mean flow around the new geometry with the 2-D Euler open-source code, the computation was performed on z planes, from which the velocity field has been then interpolated on the 3-D CAA mesh. Thus, U_z is set equal to zero in the domain, which is a proper approximation. Indeed, the vertical (radial) component of the mean flow velocity has shown to be negligible in comparison with the other velocity components by RANS solutions discussed in Sec. VI and also consistent with previous studies on realistic turbofan configurations [2]. The resulting Euler mean flowfields, in terms of axial velocity maps and streamline visualization, are plotted in Figs. 20a and 20b, respectively, for planar cuts at root and peak of the serration. The streamlines are perfectly aligned to the airfoil geometry for these two tricky positions, which should allow proper assessment of the turbulence-airfoil sources and sound propagation in the CAA.

The contour maps of the RMS pressure fluctuations on the vane skin are plotted in Fig. 21. Moreover, the strongest pressure sources are located at the roots and peaks of the serrations in accordance with

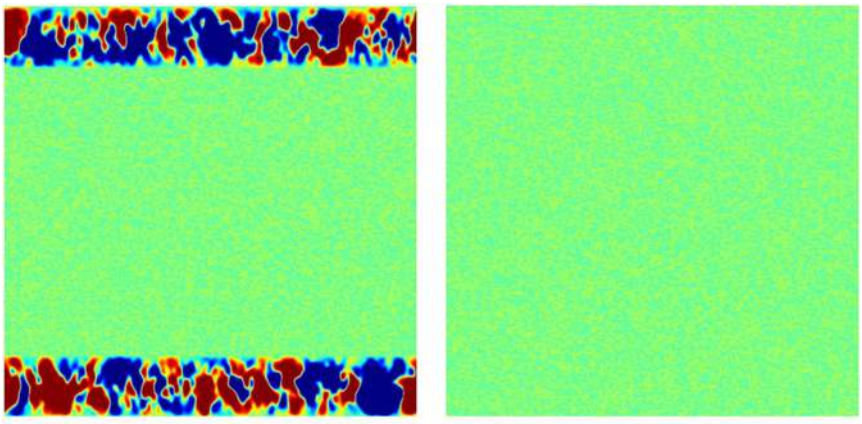

Fig. 16 At the injection surface, $\mathrm{div}(u)$ (levels between ±100 s^{-1}). Fully 3-D turbulence with a) nonzero divergence and with b) divergence-free formulation.

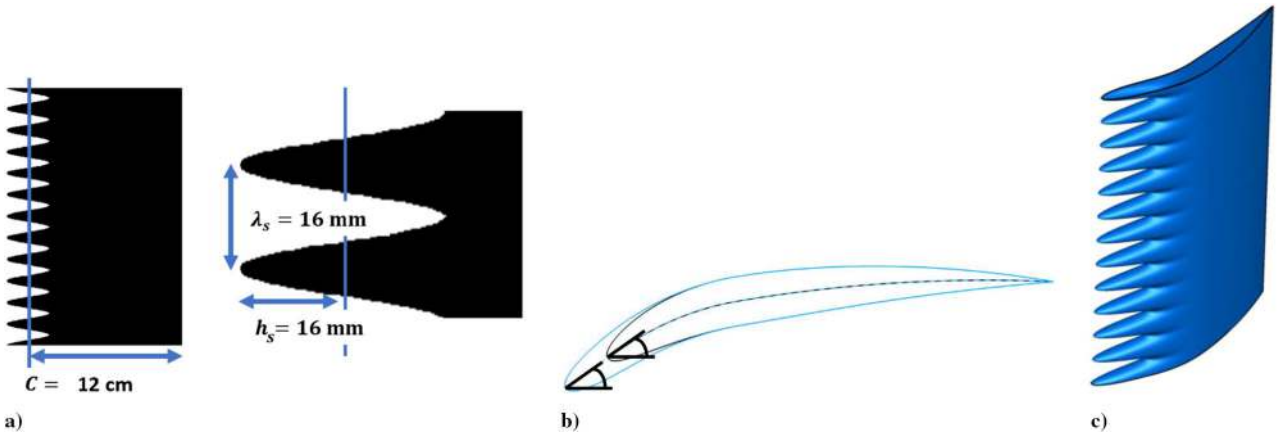

Fig. 18 The serration: a) 2D plots of the serration, b) diagram of the deformation applied on the NACA 7310, and c) 3-D geometry.

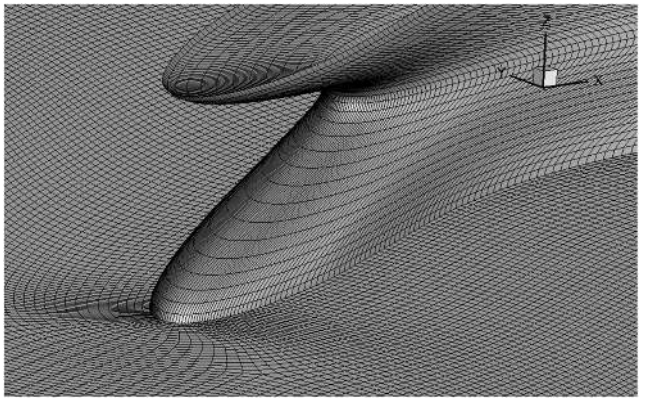

Fig. 19 Views of the skin CAA mesh and z slice at the peak of the serration.

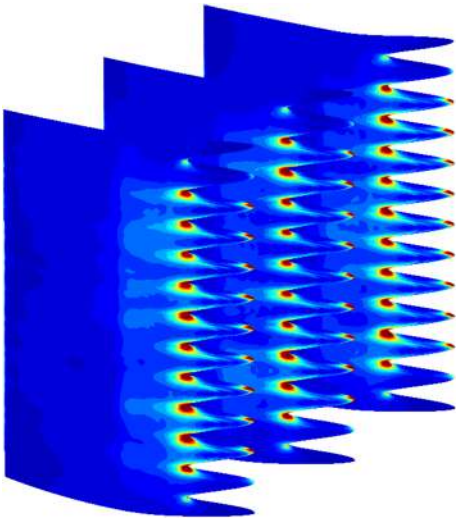

Fig. 21 RMS wall pressure p'_{rms}, Pa (levels between 0 and 500 Pa).

the literature [2,8]. Finally, the pressure fluctuations are equally distributed over the three vanes, which satisfies the periodicity conditions (enforced in the transverse direction) and indicates the good convergence of the CAA computation.

2. Sound Power-Level Reductions from CAA and Comparison with Analytical and Empirical Solutions

The noise reduction assessed in terms of sound power-level reductions (ΔPWL) spectra are summarized in Fig. 22. The numerical predictions with the different synthetic turbulence injections are compared with both an analytical solution and a semi empirical law proposed by the Institute of Sound and Vibration Research [19]. The analytical solution presented in [20] satisfies the Helmholtz advective equation and is obtained from the Wiener–Hopf technique for any piecewise leading-edge geometries. It has been slightly modified for applications to finite span airfoils in [2,5]. The semi-empirical law from [19] provides the optimal noise reduction occurring when $\lambda_s = 2L_{\xi\xi}$, for a single-wavelength geometry in terms of the Strouhal number, $\Delta\mathrm{PWL} = 10\log(St) + 10$. There is a good agreement between the different solutions in the medium frequency range, especially in comparison with the semi-empirical law. As discussed in previous numerical studies [5,29], omitting the spanwise turbulence variation leads to an overprediction of the noise reduction, particularly at high frequencies. The 3-D turbulence numerical prediction (in pink) exhibits a slightly smaller noise reduction at high frequencies compared to other CAA computations, in particular the two-wave number (k_ξ, k_z) formulation (in blue). Practically, this

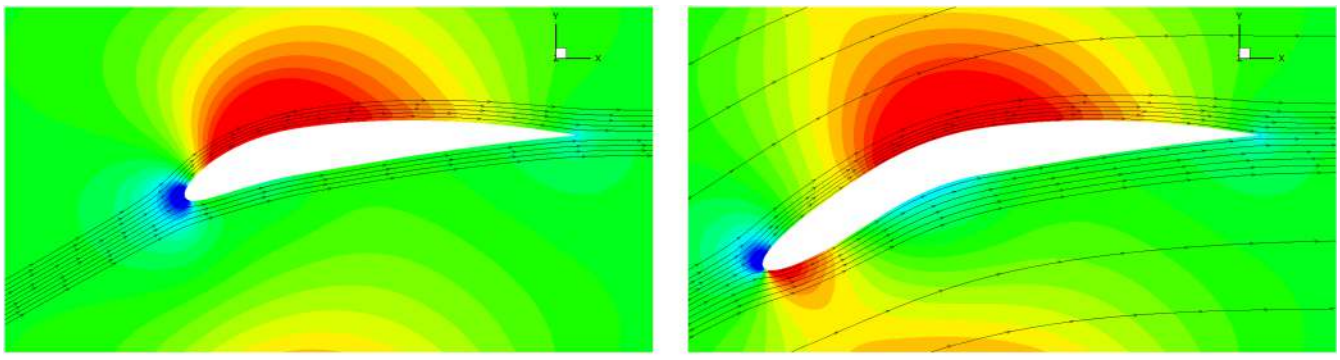

Fig. 20 Isocontour maps of U_x (levels between 60 and 120 m · s^{-1}) with streamlines. Cuts at the a) root and b) peak of the serration.

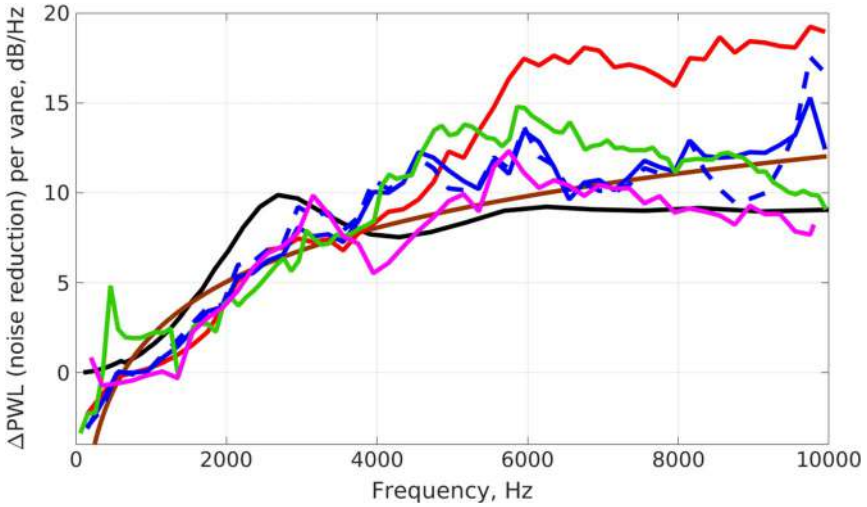

Fig. 22 Wiener–Hopf ——— and semi-empirical log law ———. Numerical spectra with a 1 kHz moving average: $k_\xi, k_z = 0$ ———, k_ξ, k_z ——— (one-channel ·····), $k_\xi, k_\eta, k_z = 0$ ———, and k_ξ, k_η, k_z ———.

study highlights that the (k_ξ, k_z) turbulence model is a good compromise in terms of accuracy versus CPU time for the noise reduction prediction. In particular, the ΔPWL spectra achieved in this case are found to be almost identical when using one-channel or three-channel simulations, which makes this approach very attractive. However, the latter conclusion should be nuanced, since it is limited to a rectilinear cascade setup.

The expected acoustic performances from numerical/analytical/semi-empirical approaches are gathered in Table 4. There is a good agreement between the trends drawn from Fig. 22 and the average noise reduction provided in Table 4. However, drawing conclusions from the overall sound power-level noise reductions (ΔOAPWL) is a bit tricky, because it is influenced by the shape of the baseline noise spectra. Indeed, due to resonance phenomena associated with periodic boundary condition (more discussed in [5]), some bumps appear in the spectra that tend to overpredict the noise emission around 500 to 1000 Hz for the three-channel setup. The later bump is a bit less visible on a multichannel computation with a turbulence invariant along the cascade directions, as shown in [5] by Fig. 15. Consequently, in order to give a better idea of the overall noise reduction for the multichannel computations, the frequency range 1300 to 9800 Hz is also considered. In any case, for all the methods, a significant ΔOAPWL (noise reduction) around 6 dB is expected.

Additionally, a parametric study has been performed using the analytical solution (based on the WH technique) in order to evaluate the acoustic performances at the three certification points (approach APP, cutback CUTB and sideline SDL). The obtained results are plotted in Fig. 23. The prediction at $M = 0.3$ (condition used for the CAA) is also given. These results show that the noise reduction is shifted towards high frequencies. As already pointed out in [2], the peak frequency of the PWL reduction roughly follows the one related to the noise emission spectrum, at respective regimes. By the way, the

Table 4 Average ΔPWL and ΔOAPWL, dB

	Average ΔPWL, 0.2 to 9.8 kHz	ΔOAPWL, 0.2 to 9.8 kHz	ΔOAPWL, 1.3 to 9.8 kHz
WH	7.3	5.5	6.8
$10\log(St) + 10$	7.5	4.9	6.1
CAA, $k_x, k_z = 0$	11.0	5.2	6.2
1-vane CAA, k_x, k_z	8.7	6.7	7.1
CAA, k_x, k_z	8.6	5.4	6.4
CAA, $k_x, k_y, k_z = 0$	9.0	3.9	5.3
CAA, k_x, k_y, k_z	7.2	3.5	5.7

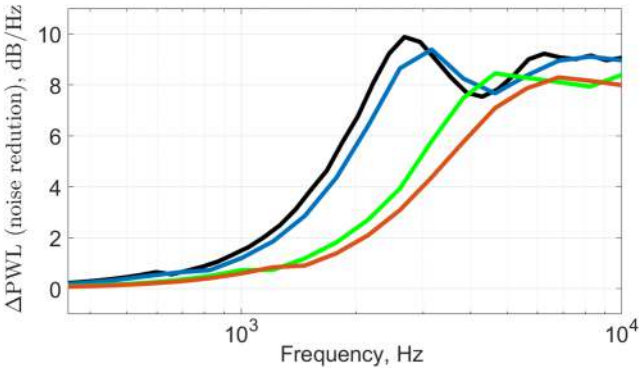

Fig. 23 Wiener–Hopf solutions at three certification points: $M = 0.3$ ———, APP ($M = 0.34$) ———, CUTB ($M = 0.53$) ———, and SDL ($M = 0.64$) ———.

low-noise design remains efficient at low-speed and high-speed flows and is thus well adapted for acoustic certification.

VI. Aerodynamic Assessment of the Serrated Design

A. RANS Simulations Setup and Aerodynamic Performance Analysis

In addition to aeroacoustic computations, an aerodynamic assessment has been conducted through RANS calculations using ONERA code elsA and applying the Jameson spatial scheme and $k - l$ Smith turbulence model. The full span extension has been considered, with the use of adiabatic walls condition on the vane and end walls and periodic boundary condition at vane channel sides. In the spanwise direction, 421 points are used, ensuring at least 30 points per serration wavelength. A view of the CFD grid containing about 5 million cells is shown in Fig. 24a. For the serrated case, the vane skin mesh (see Fig. 24b) is trimmed using the in-house modeler ersatZ, as illustrated in Fig. 25. Two operating point conditions have been investigated, at approach (APP) and at the aerodynamic design point (ADP), with inlet Mach number, respectively, equal to 0.34 and 0.67, and inlet total pressure and temperature, respectively, equal to 101,325 Pa and 288.15 K. The inflow turbulence intensity is set equal to 4.5%, and a turbulence viscosity ratio of 0.01 is considered. At APP (the selected condition for which the CAA simulations were performed), aerodynamic penalties are found to be acceptable with the first serrated design (mainly achieved for acoustics purposes) as illustrated by Fig. 26 (contour maps of Mach number). In Fig. 26, comparisons of the cut views (taken at the roots of the serration) do not reveal significant changes,

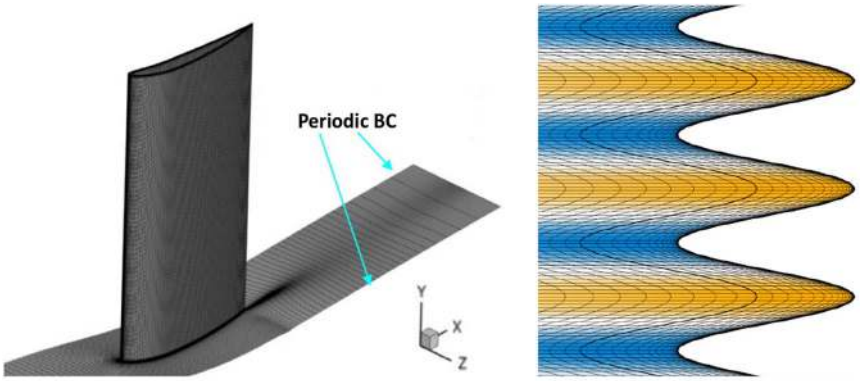

Fig. 24 CFD grid: a) one-channel mesh of the baseline CFD geometry and b) zoom view of the serrated mesh.

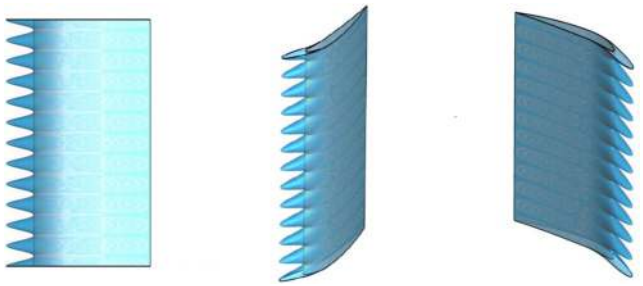

Fig. 25 Views of the baseline geometry (in gray) and the second serrated design (in blue).

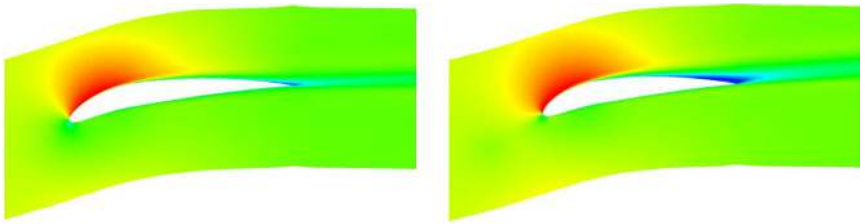

Fig. 26 Mach number (levels between 0.05 and 0.45) contour maps at APP.

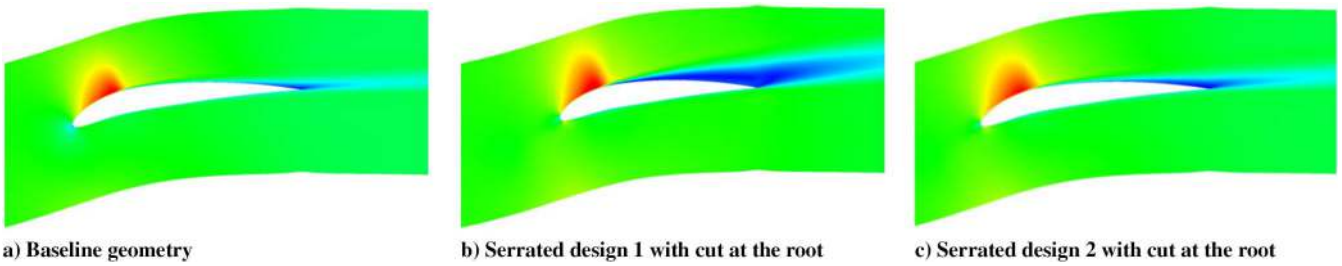

Fig. 27 Mach number (levels between 0.1 and 1.2) contour maps at ADP.

with only a slight flow separation at the trailing-edge suction side. This gives rise to a 0.14 pp (percentage points) deviation for total pressure loss coefficient and +1.8 deg deviation for outlet flow angle; see summarized results gathered in Table 5.

However, at the ADP, the aerodynamic performances are significantly deteriorated compared to the reference geometry. Indeed, contrary to the previous observations from Fig. 26, a strong flow separation is clearly shown in Fig. 27b by comparison to the baseline solution in Fig. 27a. This has resulted in the proposal of a second design presented in Sec. VI.B, consisting in a basic modification of the initial serrated design for aerodynamic purposes only.

B. Proposal of an Alternative Design to Improve Aerodynamic Behavior

In order to limit the aerodynamic penalties, more particularly pointed out at ADP, a second serrated design with an increased averaged chord (the reference chord being set at the roots) has been proposed and simulated too. Three-dimensional views of this second serrated geometry are depicted in Fig. 25. As the serration parameters h_s and λ_s are unchanged, this design 2 should have almost no impact on acoustic performances assessed with the serrated design 1. The following results address the aerodynamic performances obtained for both designs in comparison to the reference case. At APP, slightly

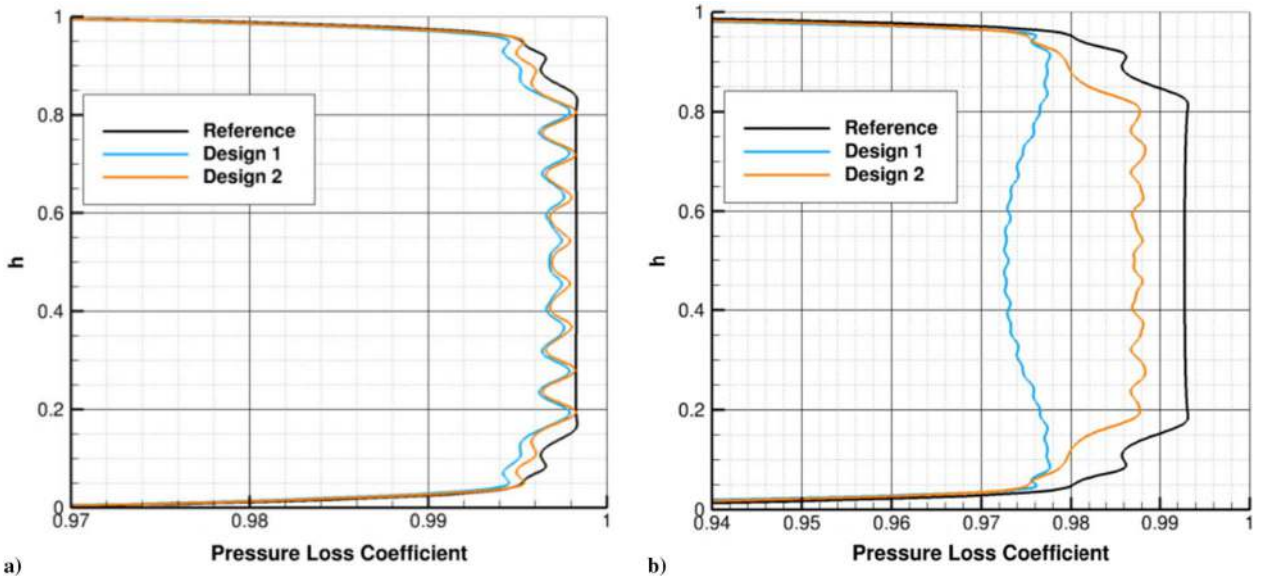

Fig. 28 Pressure loss distributions along the dimensionless spanwise coordinate $h = z/L_z$. At a) APP and b) ADP.

Table 5 Summary of the aerodynamic performances of baseline, serrated design 1, and design 2[a]

	Baseline (reference)	Design 1	Design 2
Total pressure loss coefficient at APP	0.9970	0.9956 (−0.14 pp)	0.9960 (−0.10 pp)
Total pressure loss coefficient at ADP	0.9880	0.9720 (−1.60 pp)	0.9820 (−0.60 pp)
Outlet angle (remaining swirl) at APP	2.1 deg	3.9 deg (+1.8 deg)	2.6 deg (+0.5 deg)
Outlet angle (remaining swirl) at ADP	2.5 deg	6.3 deg (+3.8 deg)	3.3 deg (+0.8 deg)

[a]Difference to the reference value in parenthesis.

better performances are obtained with the second design, as illustrated by the orange-colored pressure loss distribution in Fig. 28a. The updated penalties for total pressure loss coefficient and outlet flow angle are found to be, respectively, reduced to −0.10 pp and +0.5 deg with design 2; see Table 5. At ADP, the strong flow separation observed in Fig. 27b, is greatly reduced in the presence of design 2. The overall performances addressed in Table 5 indicate a nonsuitable penalty of −1.6 pp for total pressure loss coefficient and a flow-angle deviation of +3.8 deg with design 1. These critical values are, respectively, reduced to −0.6 pp and +0.8 deg with design 2, which is a quite valuable improvement. These positive effects are clearly pointed out on the spanwise profiles of pressure loss coefficient obtained for both designs, compared to the reference solution in Fig. 28a at APP and Fig. 28b at ADP. The benefit of using an increased mean chord is clearly highlighted, with the design 2 being able to reduce the penalties all over the span, with much more acceptable deviations of the mean flow.

VII. Conclusions

The ability to implement a fully three-dimensional turbulence with a limited computational cost has been demonstrated in this study. Wall and periodic boundary conditions have raised important challenges. To address the latter issues, a variant of the usual generation process based on the energy spectrum, similarly to [15], has been proposed. Adequately defined weighting functions have been introduced to obtain a divergence-free turbulence in the presence of wall BC. From a methodological point of view, this work has provided some additional insight on the setup of CAA computations, following on preliminary CAA simulations performed at ONERA on the InnoSTAT configuration [5]. One may conclude that multichannel computations with at least a $(k_\xi, k_\eta, k_z = 0)$ turbulence are needed to accurately reproduce the noise spectra on a baseline multichannel configurations at medium and high frequencies. The convergence at low frequencies is ensured by taking into account a large number of airfoils only, as shown in [5,33]. To simply study the relative noise reduction, a one-channel simulation with a (k_ξ, k_z) turbulence structure appears appropriate. However, in order to take into account very properly both cascade and serration effects, a 3-D synthetic turbulence might represent the best choice. The only drawback of a multichannel computation with a 3-D turbulence is that an important number of vanes has to be taken into account in order to reduce the bump at low frequency of the acoustic spectra associated with periodic boundary conditions. An alternative is to consider multichannel computations with (k_ξ, k_z) turbulence [1,2], even if the spectra are a bit altered at medium and high frequencies. The latter conclusions could be modified if other geometries were considered. In any case, the new fully 3-D turbulence methodology might be of particular interest for cases where both k_η and k_z are likely to strongly influence the acoustic sources. In parallel, a low-noise design with leading-edge serrations has been proposed, for which around 4 to 6 dB overall noise reduction can be expected at the three certification points, with a good agreement between the noise reduction spectra from the different methods. Finally, aerodynamic performances of the serrated design were evaluated. At the approach point, the design offers acceptable performance losses. However, at the ADP operating point, the aerodynamic penalties raise the need for an improved variant of the initial design. This second design, involving a larger mean chord, should not modify the acoustic prediction, since the leading-edge sinusoidal shape has been preserved. Even better, the improved aerodynamics might reduce the additional self-noise sources compared to the first design.

Appendix A: Algorithm to Determine the Direction of the Velocity for 3-D Turbulence Structures

Let us consider the wave number $\boldsymbol{k} = (k_{\xi,l}, k_{\eta,lm}, k_{z,n})^T$ in the coordinate system (ξ, η, z). The goal is to build on an orthonormal basis $(\boldsymbol{k_a}, \boldsymbol{k_b}, \boldsymbol{k_c})$ from $\boldsymbol{k}$ in order to determine $\boldsymbol{\sigma}_{lmn}$ such as $\boldsymbol{k} \cdot \boldsymbol{\sigma}_{lmn} = 0$. The main steps of the procedures are mentioned as follows with α_{lmn} a random phase term sorted for each mode (l, m, n):

1) $\boldsymbol{k_c} = \boldsymbol{k}/\|\boldsymbol{k}\|$

2) Supposing that $k_{\xi,l} > 0$

$$\begin{cases} \boldsymbol{k_a} = \left(-\dfrac{k_{\eta,lm}^2 + k_{z,n}^2}{k_{\xi,l}}, k_{\eta,lm}, k_{z,n}\right)^T_{(\xi,\eta,z)}, & \text{if } |k_{\eta,lm}| + |k_{z,n}| \neq 0 \\ \boldsymbol{k_a} = (0, k_{\eta,lm}, 0)^T_{(\xi,\eta,z)}, & \text{if } |k_{\eta,lm}| + |k_{z,n}| = 0 \end{cases}$$

3) $\boldsymbol{k_a} = \boldsymbol{k_a}/\|\boldsymbol{k_a}\|$ and $\boldsymbol{k_b} = \boldsymbol{k_b}/\|\boldsymbol{k_b}\|$
4) $\boldsymbol{k_b} = \boldsymbol{k_c} \wedge \boldsymbol{k_a}$
5) $\boldsymbol{\sigma}_{\text{lmn}} = \cos(\alpha_{\text{lmn}})\boldsymbol{k_a} + \sin(\alpha_{\text{lmn}})\boldsymbol{k_b}$, with $\alpha_{\text{lmn}} \in [0, 2\pi]$.

Appendix B: Link Between Formulations Based on the Turbulence Energy and the Velocity Autocorrelations

For the sake of simplicity, let us assume that $\beta_c = 0$. In order to achieve the comparison between the formulations, an amplitude of a given mode $u_i' = 2\sqrt{E(k)\Delta k}\sigma_i = 2\sqrt{E(k)/(2\pi k^2)\Delta k_x \Delta k_y \Delta k_z}\sigma_i$ is considered. The directivity of the velocity is given by the vector $\boldsymbol{\sigma}$, which satisfies Eq. (B1), following Appendix A:

$$\boldsymbol{\sigma} = \cos(\alpha)\frac{k}{k^2\sqrt{k_y^2 + k_z^2}}\begin{pmatrix} -(k_y^2 + k_z^2) \\ k_x k_y \\ k_x k_z \end{pmatrix} + \sin(\alpha)\frac{1}{k^2\sqrt{k_y^2 + k_z^2}}\begin{pmatrix} 0 \\ -k_z k^2 \\ k_y k^2 \end{pmatrix} \tag{B1}$$

The next step is to consider the mean value (denoted by the subscript $_{\text{mean}}$) of the squared norm of the vector $\boldsymbol{\sigma}$ from a statistical point of view, considering an infinite number of α randomly generated:

$$\sigma_x^2 = \cos^2(\alpha)\frac{1}{k^2}(k_y^2 + k_z^2)$$
$$\Rightarrow \sigma_{x,\text{mean}}^2 = \frac{1}{2}\frac{1}{k^2}(k_y^2 + k_z^2) = \frac{1}{2}\left(1 - \frac{k_x^2}{k^2}\right)$$
$$\sigma_y^2 = \frac{1}{k^4(k_y^2 + k_z^2)}(\cos(\alpha)k_x k_y k - \sin(\alpha)k_z k^2)^2$$
$$\Rightarrow \sigma_{y,\text{mean}}^2 = \frac{1}{2}\frac{1}{k^2}(k_x^2 + k_z^2) = \frac{1}{2}\left(1 - \frac{k_y^2}{k^2}\right)$$
$$\sigma_z^2 = \frac{1}{k^4(k_y^2 + k_z^2)}(\cos(\alpha)k_x k_z k + \sin(\alpha)k_y k^2)^2$$
$$\Rightarrow \sigma_{z,\text{mean}}^2 = \frac{1}{2}\frac{1}{k^2}(k_x^2 + k_y^2) = \frac{1}{2}\left(1 - \frac{k_z^2}{k^2}\right)$$

The expression of averaged (mean) velocities, with respect to α, can now be expanded:

$$u_{x,\text{mean}}'^2 = 4\frac{E(k)}{4\pi k^2}\left(1 - \frac{k_x^2}{k^2}\right)\Delta k_x \Delta k_y \Delta k_z$$
$$u_{y,\text{mean}}'^2 = 4\frac{E(k)}{4\pi k^2}\left(1 - \frac{k_y^2}{k^2}\right)\Delta k_x \Delta k_y \Delta k_z$$
$$u_{z,\text{mean}}'^2 = 4\frac{E(k)}{4\pi k^2}\left(1 - \frac{k_z^2}{k^2}\right)\Delta k_x \Delta k_y \Delta k_z$$

If one considers the squared amplitude of the average statistical velocities ($u_{i,\text{mean}}' = 2\sqrt{\varphi_{ii}\Delta k_x \Delta k_y \Delta k_z}$), the formulations that would have been obtained using autocorrelation spectra $\varphi_{ii} = E(k)/(4\pi k^2)(1 - k_i^2/k^2)$ are recovered. To conclude, it has been demonstrated that if an infinite number of modes is generated, the two formulations (relying on the energy spectrum or the autocorrelation velocity spectra) tend towards the same limit.

Appendix C: Determining Conditions Under Which a Divergence-Free Formulation Can Be Achieved

The choice has been made to alter the u_z' component, with the aim of achieving a divergence-free formulation:

$$\frac{\partial u_z'}{\partial z} = -f_w(z)A\sin(\boldsymbol{k}\cdot\boldsymbol{X} - \omega t + \psi)k_z\sigma_z + f_w'(z)A\cos(\boldsymbol{k}\cdot\boldsymbol{X} - \omega t + \psi)\sigma_z - g_w'(z)A\sigma_z \tag{C1}$$

From Eqs. (21) and (C1), one can obtain that $g_w'(z) = f_w'(z)\cos(\boldsymbol{k}\cdot\boldsymbol{X} - \omega t + \psi)$. More precisely, $g_w(z)$ is a piecewise function likewise $f_w(z)$, defined as follows:

$$\begin{cases} \forall\ z \in [z_{\min}, z_{\min} + L_w], & g_w'(z) = \dfrac{\pi}{2L_w}\sin\left(\pi\dfrac{z - z_{\min}}{L_w}\right)\cos(\boldsymbol{k}\cdot\boldsymbol{X} - \omega t + \psi) \\ \forall\ z \in [z_{\min} + L_w, z_{\max} - L_w], & g_w'(z) = 0 \\ \forall\ z \in [z_{\max} - L_w, z_{\max}], & g_w'(z) = \dfrac{\pi}{2L_w}\sin\left(\pi\dfrac{z - z_{\max}}{L_w}\right)\cos(\boldsymbol{k}\cdot\boldsymbol{X} - \omega t + \psi) \end{cases} \tag{C2}$$

The idea of the following paragraphs is to demonstrate the conditions under which the previous system of equations [Eq. (C2)] can be satisfied, taking into account that both functions f_w and g_w are C^1 and cancel in $z_{\min}$ and $z_{\max}$. Let us consider that $k_z \neq \pm\pi/L_w$ (the case $k_z = \pm\pi/L_w$, which is not detailed here, leads to the equality $\sin(k_x x + k_y y + \pi/L_w z_{\min} - \omega t + \psi) = 0$, which cannot be ensured for every set of variables):

$$\begin{cases} \forall\ z \in [z_{\min}, z_{\min} + L_w], & g_w(z) = \dfrac{-\pi^2}{2\pi^2 - 2k^2L_w^2}\cos(\boldsymbol{k}\cdot\boldsymbol{X} - \omega t + \psi)\cos\left(\pi\dfrac{z - z_{\min}}{L_w}\right) \\ & \quad - \dfrac{kL_w\pi}{2\pi^2 - 2k^2L_w^2}\sin(\boldsymbol{k}\cdot\boldsymbol{X} - \omega t + \psi)\sin\left(\pi\dfrac{z - z_{\min}}{L_w}\right) + C_a \\ \forall\ z \in [z_{\min} + L_w, z_{\max} - L_w], & g_w(z) = C_b \\ \forall\ z \in [z_{\max} - L_w, z_{\max}], & g_w(z) = \dfrac{-\pi^2}{2\pi^2 - 2k^2L_w^2}\cos(\boldsymbol{k}\cdot\boldsymbol{X} - \omega t + \psi)\cos\left(\pi\dfrac{z - z_{\max}}{L_w}\right) \\ & \quad - \dfrac{kL_w\pi}{2\pi^2 - 2k^2L_w^2}\sin(\boldsymbol{k}\cdot\boldsymbol{X} - \omega t + \psi)\sin\left(\pi\dfrac{z - z_{\max}}{L_w}\right) + C_c \end{cases} \tag{C3}$$

The integrated form of Eq. (C2) is given by Eq. (C3), in which three constants C_a, C_b, and C_c need to be determined. The functions f_w and g_w have to be damped near the boundaries, for example, at $z_{\min}$, $g_w(z_{\min}) = 0$. Thus, the constant C_a satisfies

$$C_a = \frac{\pi^2}{2\pi^2 - 2k^2L_w^2}\cos(k_x x + k_y y + k_z z_{\min} - \omega t + \psi) \tag{C4}$$

The continuity has to be ensured in $z = z_{\min} + L_w$, leading to $C_b = g_w(z_{\min} + L_w)$:

$$C_b = \frac{\pi^2}{2\pi^2 - 2k^2L_w^2}\cos(k_x x + k_y y + k_z(z_{\min} + L_w) - \omega t + \psi) + \frac{\pi^2}{2\pi^2 - 2k^2L_w^2}\cos(k_x x + k_y y + k_z z_{\min} - \omega t + \psi) \tag{C5}$$

Thus, the constant C_b can be expressed by Eq. (C5):

$$C_c = \frac{\pi^2}{2\pi^2 - 2k^2 L_w^2} \cos(k_x x + k_y y + k_z z_{\max} - \omega t + \psi) \qquad \text{(C6)}$$

Likewise at $z = z_{\max}$, $g_w(z_{\max}) = 0$, which leads to Eq. (C6):

$$C_b = \frac{\pi^2}{2\pi^2 - 2k^2 L_w^2} \cos(k_x x + k_y y + k_z (z_{\max} - L_w) - \omega t + \psi) + \frac{\pi^2}{2\pi^2 - 2k^2 L_w^2} \cos(k_x x + k_y y + k_z z_{\max} - \omega t + \psi) \qquad \text{(C7)}$$

Thereafter, $C_b = g_w(z_{\max} - L_w)$, and C_b has also to satisfy Eq. (C7):

$$\cos\left(k_x x + k_y y + k_z z_{\min} + \frac{k_z L_w}{2} - \omega t + \psi\right) \cos\left(\frac{k_z L_w}{2}\right) = \cos\left(k_x x + k_y y + k_z z_{\min} + k_z L_z - \frac{k_z L_w}{2} - \omega t + \psi\right) \cos\left(\frac{k_z L_w}{2}\right) \qquad \text{(C8)}$$

The constraint that $C_b = g_w(z_{\min} + L_w) = g_w(z_{\max} - L_w)$ imposes that Eq. (C8) has to be verified.

Acknowledgments

The present work was conducted through a collaboration within the CleanSky2 project InnoSTAT (865007) and has received funding from the European Union's Horizon 2020 research and innovation program in the frame of the Advanced Engine and Aircraft Configurations (ADEC) project of CS2 LPA-IADP.

References

[1] Cader, A., Polacsek, C., Garrec, T. L., Barrier, R., Benjamin, F., and Jacob, M., "Numerical Prediction of Rotor-Stator Interaction Noise Using 3-D CAA with Synthetic Turbulence Injection," *AIAA/CEAS Aeroacoustics Conference*, AIAA Paper 2018-4190, 2018. https://doi.org/10.2514/6.2018-4190

[2] Polacsek, C., Cader, A., Buszyk, M., Barrier, R., Gea-Aguilera, F., and Posson, H., "Aeroacoustic Design and Broadband Noise Predictions of a Fan Stage with Serrated Outlet Guide Vanes," *Physics of Fluids*, Vol. 32, No. 10, 2020, Paper 107107. https://doi.org/10.1063/5.0020190

[3] Casalino, D., Avallone, F., Gonzalez-Martino, I., and Ragni, D., "Aeroacoustic Study of a Wavy Stator Leading Edge in a Realistic Fan/OGV Stage," *Journal of Sound and Vibration*, Vol. 442, Nov. 2018, pp. 138–154. https://doi.org/10.1016/j.jsv.2018.10.057

[4] Buszyk, M., Polacsek, C., Garrec, T. L., and Barrier, R., "Lattice Boltzmann Simulations in a Rectilinear Cascade Configuration for the Turbulence-Airfoil Interaction Noise Evaluation and Reduction Through Serrated Leading Edges," *Euronoise 2021 Conference*, Sociedade Portuguesa de Acústica, 2021, pp. 359–368.

[5] Buszyk, M., Polacsek, C., and Garrec, T. L., "Assessment of a CAA Methodology for Turbulence-Cascade Interaction Noise Prediction and

Appendix D: Flow Chart Representing the Synthetic Turbulence Generation

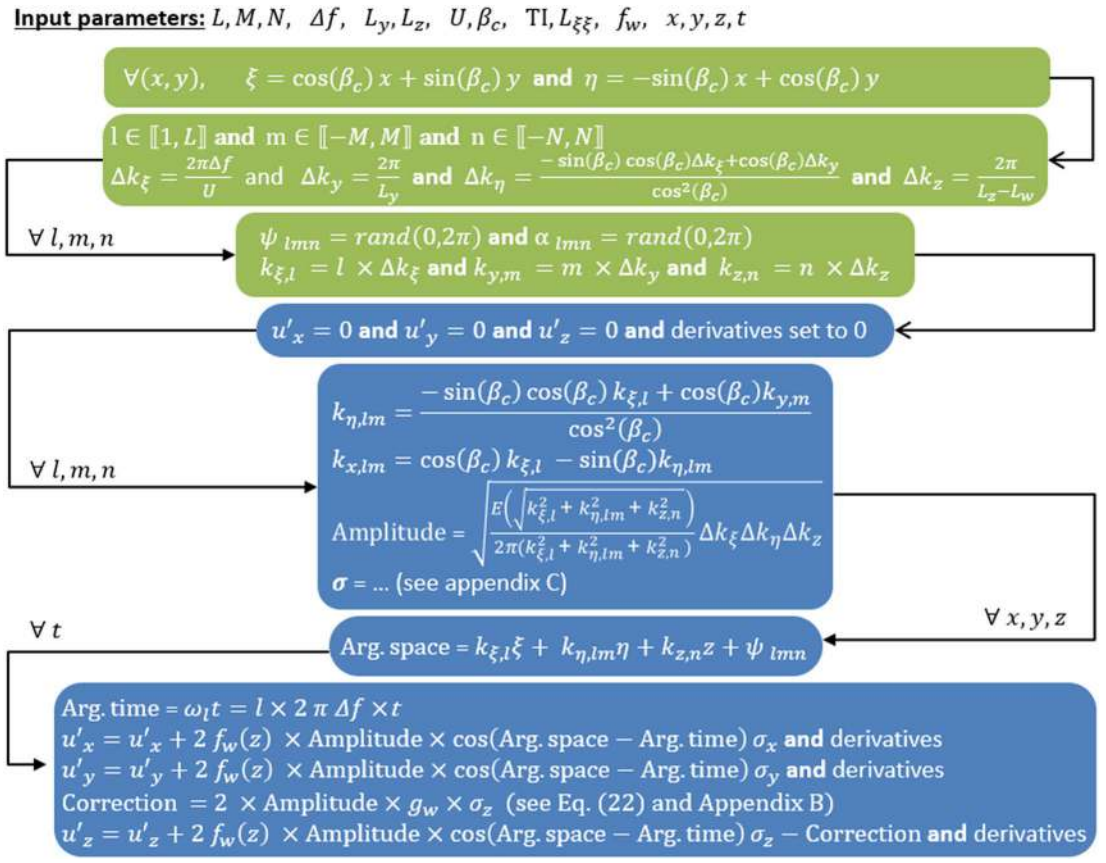

Fig. 29 Flow chart representing the synthetic turbulence generation.

Reduction from Serrated Airfoils," *eForum Acusticum 2020*, Lyon, France, 2020, pp. 2961–2968, https://hal.archives-ouvertes.fr/hal-03229464 [retrieved 13 Dec. 2021].
https://doi.org/10.48465/fa.2020.1141

[6] Kim, J. W., and Haeri, S., "An Advanced Synthetic Eddy Method for the Computation of Aerofoil–Turbulence Interaction Noise," *Journal of Computational Physics*, Vol. 287, April 2015, pp. 1–17, https://www.sciencedirect.com/science/article/pii/S0021999115000534 [retrieved 4 Feb. 2015].
https://doi.org/10.1016/j.jcp.2015.01.039

[7] Gea-Aguilera, F., Gill, J., and Zhang, X., "Synthetic Turbulence Methods for Computational Aeroacoustic Simulations of Leading Edge Noise," *Computers & Fluids*, Vol. 157, Nov. 2017, pp. 240–252.
https://doi.org/10.1016/j.compfluid.2017.08.039

[8] Gea-Aguilera, F., Gill, J., Angland, D., and Zhang, X., "Wavy Leading Edge Airfoils Interacting with Anisotropic Turbulence," *23rd AIAA/CEAS Aeroacoustics Conference*, AIAA Paper 2017-3370, 2017.
https://doi.org/10.2514/6.2017-3370

[9] Gea-Aguilera, F., Karve, R., Gill, J., Zhang, X., and Angland, D., "On the Effects of Anisotropic Turbulence on Leading Edge Noise," *Journal of Sound and Vibration*, Vol. 495, March 2021, Paper 115895, https://www.sciencedirect.com/science/article/pii/S0022460X20307343.
https://doi.org/10.1016/j.jsv.2020.115895

[10] Ewert, R., Dierke, J., Siebert, J., Neifeld, A., Appel, C., Siefert, M., and Kornow, O., "CAA Broadband Noise Prediction for Aeroacoustic Design," *Journal of Sound and Vibration*, Vol. 330, No. 17, 2011, pp. 254–263.
https://doi.org/10.1016/j.jsv.2011.04.014

[11] Kissner, C. A., and Guérin, S., "Fan Broadband Noise Prediction for the ACAT1 Fan Using a Three-Dimensional Random Particle Mesh Method," AIAA Paper 2020-2520, 2020.
https://doi.org/10.2514/6.2020-2520

[12] Kissner, C. A., and Guérin, S., "Comparison of Predicted Fan Broadband Noise Using a Two- Versus a Three-Dimensional Synthetic Turbulence Method," *Journal of Sound and Vibration*, Vol. 508, No. 3, 2021, Paper 116221.
https://doi.org/10.1016/j.jsv.2021.116221

[13] Kraichnan, R., "Diffusion by a Random Velocity Field," *Physics of Fluids*, Vol. 13, Jan. 1970, pp. 22–31.
https://doi.org/10.1063/1.1692799

[14] Bechara, W., Bailly, C., Lafon, P., and Candel, S., "Stochastic Approach to Noise Modeling for Free Turbulent Flows," *AIAA Journal*, Vol. 32, March 1994, pp. 455–463.
https://doi.org/10.2514/3.12008

[15] Gill, J. S., Zhang, X., and Joseph, P. F., "Single Velocity-Component Modeling of Leading Edge Turbulence Interaction Noise," *Journal of the Acoustical Society of America*, Vol. 137, No. 6, 2015, pp. 3209–3220.
https://doi.org/10.1121/1.4921547

[16] Amiet, R. K., "High Frequency Thin-Airfoil Theory for Subsonic Flow," *AIAA Journal*, Vol. 14, No. 8, 1976, pp. 1076–1082.
https://doi.org/10.2514/3.7187

[17] Niedoba, P., Jicha, M., and Čermák, L., "On Stochastic Inlet Boundary Condition for Unsteady Simulations," *European Physical Journal Conferences*, Vol. 67, Feb. 2014, pp. 495–498.
https://doi.org/10.1051/epjconf/20146702082

[18] Reboul, G., Cader, A., Polacsek, C., Garrec, T. L., Barrier, R., and Nasr, N. B., "CAA Prediction of Rotor-Stator Interaction Using Synthetic Turbulence: Application to a Low-Noise Serrated OGV," AIAA Paper 2017-3714, 2017.
https://doi.org/10.2514/6.2017-3714

[19] Paruchuri, C., Joseph, P., Narayanan, S., Vanderwel, C., Turner, J., Kim, J. W., and Ganapathisubramani, B., "Performance and Mechanism of Sinusoidal Leading Edge Serrations for the Reduction of Turbulence–Aerofoil Interaction Noise," *Journal of Fluid Mechanics*, Vol. 818, May 2017, p. 435–464.
https://doi.org/10.1017/jfm.2017.141

[20] Ayton, L., and Paruchuri, C., "An Analytical and Experimental Investigation of Aerofoil–Turbulence Interaction Noise for Plates with Spanwise-Varying Leading Edges," *Journal of Fluid Mechanics*, Vol. 865, April 2019, pp. 137–168.
https://doi.org/10.1017/jfm.2019.78

[21] Redonnet, S., Manoha, E., and Sagaut, P., "Numerical Simulation of Propagation of Small Perturbations Interacting with Flows and Solid Bodies," AIAA Paper 2001-2223, 2001.
https://doi.org/10.2514/6.2001-2223

[22] Clair, V., "Calcul Numérique de la Réponse Acoustique d'un Aubage Soumis à un Sillage Turbulent," Ph.D. Dissertation, Laboratoire de Mécanique des Fluides et d'Acoustique (LMFA), Ecole centrale de Lyon, France, 2013.

[23] Tam, C. K. W., and Dong, Z., "Radiation and Outflow Boundary Conditions for Direct Computation of Acoustic and Flow Disturbances in a Nonuniform Mean Flow," *Journal of Computational Acoustics*, Vol. 4, No. 2, 1996, pp. 175–201.
https://doi.org/10.1142/S0218396X96000040

[24] Blazek, J., Computational Fluid Dynamics 3rd Edition. Principles and Applications, Butterworth-Heinemann, Germany, 2015, pp. 398–399.

[25] Ffowcs Williams, J. E., Hawkings, D. L., and Lighthill, M. J., "Sound Generation by Turbulence and Surfaces in Arbitrary Motion," *Philosophical Transactions of the Royal Society of London. Series A, Mathematical and Physical Sciences*, Vol. 264, No. 1151, 1969, pp. 321–342.
https://doi.org/10.1098/rsta.1969.0031

[26] Reboul, G., "Modélisation du Bruit à large Bande de SOUFFLANTES de Turboréacteurs," Ph.D. Dissertation, Laboratoire de Mécanique des Fluides et d'Acoustique (LMFA), Ecole Centrale de Lyon, Nov. 2010, https://tel.archives-ouvertes.fr/tel-00562647 [retrieved 14 Sept. 2021].

[27] Liepmann, H. W., Laufer, J., and Liepmann, K., *On the Spectrum of Isotropic Turbulence*, NACA, Washington, D.C., 1951.

[28] Glegg, S., and Devenport, W., "Chapter 9—Turbulent Flows," *Aeroacoustics of Low Mach Number Flows*, edited by S. Glegg, and W. Devenport, Academic Press, New York, 2017, pp. 185–220, https://www.sciencedirect.com/science/article/pii/B9780128096512000096 [retrieved 31 Dec. 2017].
https://doi.org/10.1016/B978-0-12-809651-2.00009-6

[29] Clair, V., Polacsek, C., Garrec, T. L., Reboul, G., Gruber, M., and Joseph, P., "Experimental and Numerical Investigation of Turbulence-Airfoil Noise Reduction Using Wavy Edges," *AIAA Journal*, Vol. 51, Nov. 2013, pp. 2695–2713.
https://doi.org/10.2514/1.J052394

[30] Glegg, S., "The Response of a Swept Blade Row to a Three-Dimensional Gust," *Journal of Sound and Vibration*, Vol. 227, Oct. 1999, pp. 29–64.
https://doi.org/10.1006/jsvi.1999.2327

[31] Hanson, D., and Horan, K., "Turbulence/Cascade Interaction—Spectra of Inflow, Cascade Response, and Noise," *4th AIAA/CEAS Aeroacoustics Conference*, AIAA Paper 1998-2319, June 1998.
https://doi.org/10.2514/6.1998-2319

[32] Blandeau, V., Joseph, P., Jenkins, G., and Powles, C., "Comparison of Sound Power Radiation from Isolated Airfoils and Cascades in a Turbulent Flow," *Journal of the Acoustical Society of America*, Vol. 129, June 2011, pp. 3521–30.
https://doi.org/10.1121/1.3569706

[33] Gea-Aguilera, F., "Aerodynamic and Aeroacoustic Modelling of Engine Fan Broadband Noise," Ph.D. Dissertation, Faculty of Engineering and the Environment—Airbus Noise Technology Centre, Univ. of Southampton, England, U.K., 2017.

[34] Paruchuri, C., "Aerofoil Geometry Effects on Turbulence Interaction Noise," Ph.D. Dissertation, Faculty of Engineering and the Environment, Univ. of Southampton, England, U.K., April 2017, https://eprints.soton.ac.uk/415884/ [retrieved 11 Dec. 2021].